Network-Based Fractional-Order Control Algorithms for Vehicle Platooning

IEEE Access
Multidisciplinary | Rapid Review | Open Access Journal

Received 4 July 2025, accepted 24 July 2025, date of publication 4 August 2025, date of current version 13 August 2025.

*Digital Object Identifier 10.1109/ACCESS.2025.3595116*

RESEARCH ARTICLE

# Network-Based Fractional-Order Control Algorithms for Vehicle Platooning

**OMAR HANIF[1], (Graduate Student Member, IEEE), PATRICK GRUBER[1], ALDO SORNIOTTI[2], (Member, IEEE), AND UMBERTO MONTANARO[1]**

[1]Centre for Aerodynamics, Aerospace and Automotive Engineering, School of Engineering, University of Surrey, GU2 7XH Guildford, U.K.
[2]Department of Mechanical and Aerospace Engineering, Politecnico di Torino, 10129 Turin, Italy

Corresponding author: Umberto Montanaro (u.montanaro@surrey.ac.uk)

This work was supported by the Engineering and Physical Sciences Research Council (EPSRC) under Project 2757376.

**ABSTRACT** Fractional-order controllers have been shown to be an effective solution for improving the tracking performance of closed-loop control systems in various engineering applications. However, the use of fractional-order solutions has only been marginally investigated for controlling platoons of vehicles. Hence, this paper proposes three novel distributed fractional-order controllers, in which the vehicle platooning control problem of a set of homogeneous followers, characterised by either second- or third-order systems, is reformulated as a consensus control problem. The resulting closed-loop systems are analysed using the root locus approach to determine the region of control gains that ensures asymptotic closed-loop stability. Furthermore, the residual spacing errors to constant leader accelerations and disturbances are computed by analysing the error dynamics in the Laplace domain. The genetic algorithm is then employed for parameter optimisation within the stable region for different scenarios, and numerical analysis supports the theoretical findings and shows reduced tracking error when the fractional-order solutions replace their integer-order counterparts.

**INDEX TERMS** Vehicle platooning, fractional-order control, cooperative control.

## I. INTRODUCTION

An autonomous vehicle platoon is a cooperative driving scenario. In such a scenario, a string of consecutive connected autonomous vehicles (CAVs) travels at the speed of the first vehicle, also known as a leader, while also controlling the intervehicular distance to a desired value. The leader is responsible for setting the platoon speed, acceleration and trajectory, respectively. The subsequent vehicles, also known as followers, synchronise their motion to that of the leader based on the data received from the neighbouring vehicles through a communication network.

Vehicle platooning offers several transportation as well as environmental benefits. These range from reduced energy consumption for the fleet to improving safety and comfort while increasing road efficiency [1], [2]. To achieve the aforementioned benefits, there is a need to tightly control the cooperative platoon motion through control systems.

The associate editor coordinating the review of this manuscript and approving it for publication was Liang-Bi Chen.

In this framework, vehicle platoon control solutions can be characterised through the four-component framework [3]. According to this framework, the key ingredients of any platoon control system are: (i) node dynamics (ND), which model the longitudinal dynamics of each vehicle; (ii) the information flow topology (IFT), detailing the communication pattern among vehicles in the platoon; (iii) formation geometry (FG), describing the inter-vehicular distance policy between consecutive vehicles; and (iv) distributed controllers (DC), which locally decide the control action of each vehicle based on the information of other platoon vehicles gathered through the network. See Figure 1, which summarises the four-component framework. The longitudinal vehicle model (Node Dynamics) can be represented as nonlinear, capturing detailed vehicle dynamics, or simplified as linear through linearisation for computational efficiency. Typically, second or third-order linear node models are used in vehicle platoon control design, as they balance accuracy and complexity [4]. Similarly, several Information Flow Topologies (IFTs) have been used in the literature. Common IFTs include predecessor

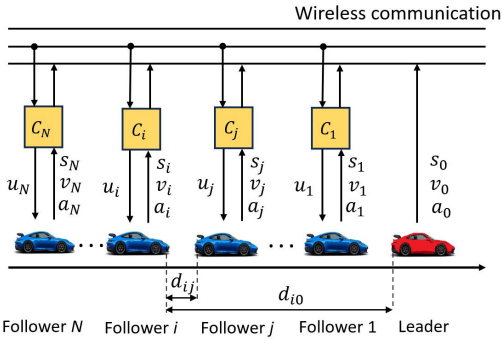


**FIGURE 1.** An illustrative representation of the four-component framework.

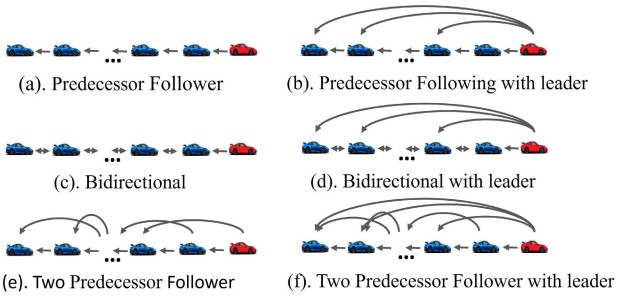


**FIGURE 2.** Common information flow topologies.

follower (PF), predecessor follower with leader (PFL), bidirectional (BD), bidirectional with leader (BDL), two predecessor follower (TPF), and two predecessor follower with leader (TPFL) [5]. Figure 2 illustrates six common topologies: (a) PF, where each vehicle communicates only with its immediate predecessor; (b) PFL, which builds on PF by adding leader-to-all the followers broadcasts; (c) BD, where vehicles exchange information with both their immediate predecessor and successor; (d) BDL, which augments BD with leader-to-follower links; (e) TPF, in which each vehicle receives data from its immediate predecessor as well as the vehicle two positions ahead; and (f) TPFL, which extends TPF by incorporating direct leader-to-follower communication.

Over the past decade, Distributed Controllers (DCs) have evolved considering various communication topologies. Consequently, the controller design is inherently shaped by these network structures. Initially, research primarily focused on developing control algorithms tailored to specific IFTs such as PF [6], PFL [7], [8], BD [9], BDL [10], etc. However, by recasting the cooperative platoon control motion as a synchronisation/consensus control problem of a network of dynamic systems, it is possible to devise distributed control strategies applicable to a wider range of topologies that satisfy a set of conditions (i.e., undirected topologies, e.g., BD, BDL, etc. [11], [12]; directed topologies with a spanning tree rooted on the leader, e.g., PF, PFL, etc. [13]). The control algorithms originally developed for single-agent systems have been systematically extended to distributed control algorithms for multi-agent systems, particularly for vehicle platooning. Examples of these distributed control algorithms include distributed linear control [14], distributed adaptive control [15], robust $H_\infty$ control [16], distributed sliding mode control [17], and distributed model predictive control [18], etc., as shown in Figure 1. These algorithms build upon the theory of synchronisation in dynamic systems [19], [20], which provides a foundation for coordinated behaviour in vehicle platoons.

Fractional-order control (FOC) enhances traditional control by applying principles of the fractional calculus, offering more design flexibility to achieve the desired control objective. This, in turn, improves closed-loop performance, such as reference tracking, and disturbance rejection [21], [22]. FOC has demonstrated benefits in many stand-alone or single-agent systems when compared to integer-order control techniques. For example, FOC approaches handle uncertainties in the frequency control of the power system load [23], [24], with relocated fractional internal model control strategies employed for communication latency mitigation [25] and achieve precise pressure control in medical devices [21]. Superior performance is also documented in industrial processes [26], [27], [28], including fractional-order controllers for nonlinear distillation column systems [29]; integrating systems with time delays [22], [30], [31], and stabilising nonlinear systems such as inverted pendulums [32]. Fractional-order PID-based controllers include Tilt-Integral-Derivative (TID) [31], [33], [34], Fractional-Order Proportional-Derivative (FOPD) [35], [36], and Fractional-Order Proportional-Integral-Derivative (FOPID) strategies [21], [37], [38], [39], and have been shown to enhance design flexibility [40], [41], [42]. These fractional order PID variants also offer better reference tracking, transient responses and disturbance rejection as compared to the conventional controllers.

Besides modelling and controlling of the single agent systems, extensive research has been conducted on the integer-order control of multi-agent systems (MAS) with fractional-order node dynamics. Recent studies in this area include [43], [44], [45], [46]. However, only a few studies have focused on designing fractional-order controllers for MAS having integer-order node dynamics. The work presented in [47], [48] introduces fractional-order proportional-integral (FOPI) controllers, which improve convergence performance for networks of single and double integrators. Fractional PID controllers have been investigated in [49] for MAS with second-order node dynamics. Fractional-order sliding-mode control has been shown to guarantee finite-time convergence in multi-agent systems comprising nonholonomic wheeled mobile robots, where the individual agent dynamics are modelled using integer-order differential equations [50], [51]

Despite progress in the development of distributed control algorithms for MAS, fractional order-based controllers for vehicle platooning have only been marginally explored.

The author of [52] introduced a distributed fractional-order control for the platoon communicating in a PF topology, achieving robustness against uncertainty and noise. In [53], the authors developed a fractional-order control featuring an iso-damping property that maintains consistent closed-loop stability despite variations in vehicle plant gains. Extending the earlier work by the same authors in [54], they developed fractional-order control, which effectively handled communication delays inherent in communication for the PF topology. The authors of [55] developed a fractional-order controller for the platoon using bidirectional topologies, providing resilience against adversarial gain modification attacks. The authors in [56] developed an adaptive fractional-order PID controller for longitudinal control of vehicles in a platoon in PF topology. The proposed adaptive mechanism enables the adjustment of the parameters to accommodate uncertainties.

Hence, to the best of the authors' knowledge, the current application of fractional-order controllers to vehicle platooning is limited to the use of a specific network topology. This paper addresses this gap through the following contributions:

1) the design of three network-based fractional-order controllers—TID, FOPD and FOPID— for vehicle platooning, which can be applied to any network topology with positive information flow matrix;
2) the closed-loop analysis of the stability region of each control solution via the Root Boundary Locus (RBL) method;
3) an extensive simulation analysis targeting *(i)* a quantitative comparison of the closed-loop tracking performance provided by the novel fractional-order control solutions with respect to their integer-order counterparts across different topologies and platoon lengths, and *(ii)* a robustness analysis to uncertain nonlinear heterogeneous vehicles dynamics.

The paper is organised as follows: Section II provides the formulation of the platoon control problem as a synchronisation of a network of dynamic systems, as well as modelling the node dynamics and network. Section III presents the design of three decentralised fractional-order controllers (DFOCs) for vehicle platooning, along with the main theorems. The proofs of theorems are detailed in Sections IV, V and VI. Section VII presents results from different simulation analyses and compares the performance of the proposed DFOCs with conventional control strategies. Conclusions are drawn in Section VIII. In addition, for the sake of completeness, Appendix A reports key definitions in the context of fractional calculus used within the paper, while Appendix B provides an overview of the RBL method used to guarantee closed-loop stability of the proposed control methods.

## II. PLATOON CONTROL PROBLEM AS SYNCHRONISATION OF A DYNAMIC NETWORK

The vehicle platooning control problem can be recast as the synchronisation of a network of dynamic systems with a pinning node, where the dynamics of each node are those of the follower while the pinner dynamics are those of the leader. Moreover, the pattern through which vehicles in the platoon share information is the network topology and the control action implemented by each follower to achieve the platoon cooperative motion is the network protocol [57]. In what follows, the node dynamics (vehicle dynamics) and the key definitions related to the modelling of network topology used in the rest of the paper are given.

### A. LONGITUDINAL NODE DYNAMICS

For the design of distributed control strategies for vehicle platooning, linear longitudinal vehicle dynamics (node dynamics) are usually used [57]. It is noted that despite the vehicle longitudinal dynamics being nonlinear, low-level control algorithms are used to linearise them for vehicle platoon control design [58]. Specifically, the node dynamics are often modelled as either second or third-order linear systems. In case of second-order linear systems, the node dynamics are [59], [60].

$$\dot{s}_i(t) = v_i(t), \quad \dot{v}_i(t) = u_i(t) + w_i, \tag{1}$$

where $s_i$ and $v_i$ are the position and velocity of the $i$-th vehicle, respectively, with $i = 0, 1, \ldots, N$, where $N$ is the number of followers in the platoon and $i = 0$ represents the leader vehicle. In system (1), $u_i$ is the acceleration of the $i$-th follower for $i = 1, \ldots, N$, and $w_i$ represents external disturbances acting on the $i$-th follower. In the case of a third-order system, the dynamics of each vehicle are given as reported in [61]:

$$\dot{s}_i(t) = v_i(t), \tag{2a}$$
$$\dot{v}_i(t) = a_i(t), \tag{2b}$$
$$\dot{a}_i(t) = -\frac{1}{\tau}a_i(t) + \frac{1}{\tau}u_i(t) + \frac{1}{\tau}w_i, \tag{2c}$$

where $a_i$ is the acceleration of the $i$-th vehicle, $u_i$ is the desired vehicle acceleration, and $\tau$ is the powertrain time lag assumed to be the same for each vehicle (homogeneous vehicle platooning). The disturbance that acts on each vehicle is collected in the vector $\bar{w}$:

$$\bar{w} = \begin{bmatrix} w_1 & w_2 \ldots & w_N \end{bmatrix}^T \in \mathbb{R}^N. \tag{3}$$

## III. MODELLING OF NETWORK TOPOLOGY

The network topology in the platoon $\mathcal{N}$ followers is represented by a graph $\mathcal{G}_N = (\mathcal{V}_N, \mathcal{E}_N)$ where $\mathcal{V}_N = \{1, 2, \ldots, N\}$ are the vertices of the node set of the network, and $\mathcal{E}_N \subseteq \mathcal{V}_N \times \mathcal{V}_N$ is the set of arcs or the edges of the network. For the $i$-th vehicle getting the information from the $j$-th vehicle, $(j, i) \in \mathcal{E}_N$. Algebraically, the network topology is represented by the adjacency matrix $\mathcal{A}_N = [\tilde{a}_{ij}]_{i,j=1,\ldots,N}$, where $\tilde{a}_{ij} = 1$ if $(j, i) \in \mathcal{E}_N$ and it is zero otherwise. The Laplacian matrix for the graph $\mathcal{G}_N$, denoted by $\mathcal{L} = [l_{ij}]_{i,j=1,\ldots,N}$ is defined as:

$$\mathcal{L} = \begin{cases} -\tilde{a}_{ij}, & i \neq j, \\ \sum_{k=1,k\neq i}^{N} \tilde{a}_{ik}, & i = j. \end{cases} \tag{4}$$

The Laplacian can also be computed as:

$$\mathcal{L} = \mathcal{D} - \mathcal{A}_N, \tag{5}$$

where $\mathcal{D}$ is the in-degree matrix, and the $i$-th entry on the diagonal is computed as $\sum_{j=1}^{N} \tilde{a}_{ij}$. The information flow between the leader and followers is modelled by the pinning matrix $\mathcal{P} \in \mathbb{R}^{N\times N}$, which is mathematically expressed as:

$$\mathcal{P} = \text{diag}(p_1, p_2, \ldots, p_N), \tag{6}$$

where $p_i = 1$ if and only if the edge $(0, i) \in \mathcal{E}_{N+1}$, i.e., vehicle $i$ is pinned to the leader. The information matrix is defined as reported in [62]:

$$\mathcal{H} = \mathcal{L} + \mathcal{P}. \tag{7}$$

In the rest of the paper, it is assumed that the information matrix has real eigenvalues. This assumption is not restrictive as it is satisfied by topologies usually used for the design of vehicle platoon control solutions, whose $\mathcal{H}$ is either symmetric or triangular [63]. Furthermore, it is assumed that the topology has a spanning tree rooted at the leader node (node zero). Under this assumption, the information matrix $\mathcal{H}$ is strictly positive, i.e., $\lambda_i > 0$, with $\lambda_i$, $i = 1, 2, \ldots, N$ being its $i^{\text{th}}$ eigenvalue [63]. Consequently, there exists an invertible matrix such that it can be decomposed into Jordan canonical form as [63], [64]:

$$\mathcal{H} = \mathcal{V}\Lambda\mathcal{V}^{-1}, \tag{8}$$

where $\mathcal{V}$ is an invertible square matrix and $\Lambda = \text{diag}(\lambda_1, \lambda_2, \ldots, \lambda_N)$. Furthermore, $\min(\lambda_i)$ and $\max(\lambda_i)$ denote the minimum and the maximum eigenvalue of $\mathcal{H}$, respectively.

### A. CONTROL OBJECTIVE

The platoon control problem consists of two main objectives:
1. Synchronisation of the states of the vehicles in the platoon.
2. Maintaining the desired intervehicular distance between the $i$-th and $j$-th vehicles according to the chosen spacing policy. Mathematically, when the second order vehicle dynamics (1) are adopted, platoon control objective [65] is:

$$\lim_{t\to+\infty} \|s_i - s_j - d_{ij}\| = 0, \quad \lim_{t\to+\infty} \|v_i - v_0\| = 0, \tag{9}$$

where $d_{ij}$ is the desired constant distance between the $i$-th and $j$-th vehicles. In the case of third-order dynamics (2) are used to model the nodes, the vehicle platoon control problem [66] is:

$$\lim_{t\to+\infty} \|s_i - s_j - d_{ij}\| = 0, \tag{10}$$

$$\lim_{t\to+\infty} \|v_i - v_0\| = 0, \tag{11}$$

$$\lim_{t\to+\infty} \|a_i - a_0\| = 0, \tag{12}$$

where $a_0$ is the constant acceleration of the leader. The mismatch between the leader and follower states is defined as:

$$\tilde{s} = \begin{bmatrix}\tilde{s}_1 & \tilde{s}_2 & \ldots & \tilde{s}_N\end{bmatrix}^T, \tag{13a}$$

$$\tilde{v} = \begin{bmatrix}\tilde{v}_1 & \tilde{v}_2 & \ldots & \tilde{v}_N\end{bmatrix}^T, \tag{13b}$$

$$\tilde{a} = \begin{bmatrix}\tilde{a}_1 & \tilde{a}_2 & \ldots & \tilde{a}_N\end{bmatrix}^T, \tag{13c}$$

where $\tilde{s}_i = s_i - s_0 - d_{i0}$, $\tilde{v}_i = v_i - v_0$, $\tilde{a}_i = a_i - a_0$, and $d_{i0}$ is the desired intervehicular distance between the leader and the $i^{\text{th}}$ follower, with $i = 1, 2, \ldots, N$. Moreover, in the rest of the paper, the vector $\bar{a}_0$ is defined as:

$$\bar{a}_0 = a_0 \cdot \begin{bmatrix}1 & 1 & \ldots & 1\end{bmatrix}^T \in \mathbb{R}^N. \tag{14}$$

## IV. FRACTIONAL-ORDER DISTRIBUTED CONTROLLERS DESIGN

In this paper, three fractional-order extensions of distributed PID control strategies are presented, which include fractional-order control terms for node dynamics modelled as either second-order or third-order systems. These algorithms are named as distributed: (i) Fractional-Order Proportional-Integral-Derivative (FOPID), (ii) Tilt Integral Derivative (TID), and (iii) Fractional-Order Proportional Derivative (FOPD) and are presented in the rest of the section along with the corresponding main theorems.

### A. DISTRIBUTED FOPID CONTROL STRATEGY

In the case of the distributed FOPID strategy, the follower computes the control action as:

$$\begin{aligned} u_{i\text{FOPID}}(t) = -\Bigg\{ & \sum_{j=1}^{N} \tilde{a}_{ij} \Big( K_P \left(s_i(t) - s_j(t) - d_{ij}\right) \\ & + K_I \int_0^t \left(s_i(\zeta) - s_j(\zeta) - d_{ij}\right) d\zeta \\ & + K_D\, {}_0D_t^{\mu} \left(s_i(t) - s_j(t) - d_{ij}\right) \Big) \\ & + p_i \Big( K_P \left(s_i(t) - s_0(t) - d_{i0}\right) \\ & + K_I \int_0^t \left(s_i(\zeta) - s_0(\zeta) - d_{i0}\right) d\zeta \\ & + K_D \Big( {}_0D_t^{\mu} \left(s_i(t) - s_0(t) - d_{i0}\right) \Big) \Big) \Bigg\}, \end{aligned} \tag{15}$$

where $K_P$, $K_I$, and $K_D$ are the control gains, and $\mu \in (0, 2)$ is the fractional-order parameter.

*Theorem 1 (FOPID):* Consider a homogeneous platoon of vehicles with $N$ followers, node dynamics given in (1), and the acceleration of the leader and the disturbance vector $w$ being constants (either zero or different from zero). Assume that the information matrix $\mathcal{H}$ is strictly positive and has real eigenvalues. If the control gains of the FOPID strategy are chosen such that the following conditions hold:

$$K_D > 0, \tag{16a}$$

$$K_P > \frac{\left(\frac{K_I}{K_D \sin(\mu\pi/2)}\right)^{\frac{2}{\mu+1}}}{\min(\lambda_i)} - K_D \left(\frac{K_I}{K_D \sin(\mu\pi/2)}\right)^{\frac{\mu}{\mu+1}} \cos(\mu\pi/2), \tag{16b}$$

$$K_I > 0. \tag{16c}$$

then the FOPID algorithm guarantees the asymptotic stability of the closed-loop system, and the intervehicular distance and velocity errors converge to zero (i.e., Eqs. (9) hold).

### B. DISTRIBUTED FOPD CONTROL STRATEGY

In the case of the distributed FOPD strategy, the follower computes the control action as:

$$\begin{aligned} u_{i\mathrm{FOPD}}(t) = -\Bigg\{ & \sum_{j=1}^{N} \tilde{a}_{ij} \Big( K_P \left( s_i(t) - s_j(t) - d_{ij} \right) \\ & + K_D \Big( {}_0D_t^{\mu} \left( s_i(t) - s_j(t) - d_{ij} \right) \Big) \Big) \\ & + p_i \Big( K_P \left( s_i(t) - s_0(t) - d_{i0} \right) \\ & + K_D \Big( {}_0D_t^{\mu} \left( s_i(t) - s_0(t) - d_{i0} \right) \Big) \Big) \Bigg\}, \end{aligned} \tag{17}$$

where $K_P$ and $K_D$ are control gains to be tuned.

*Theorem 2 (FOPD):* Consider a homogeneous platoon of vehicles with $N$ followers, node dynamics given in (2), and the acceleration of the leader and the disturbance vector $w$ being constants. Assume that the information matrix $\mathcal{H}$ is strictly positive and has real eigenvalues, and $\mu \in (0, 2)$. If the control gains of the FOPD strategy are chosen such that the following conditions hold for different ranges of $\mu$:

For $0 < \mu < 1$:

$$0 < K_D < \frac{\left(\sin\left(\frac{\mu\pi}{2}\right)\right)^{2-\mu}}{\tau^{2-\mu} \max(\lambda_i) \left(\cos\left(\frac{\mu\pi}{2}\right)\right)^{3-\mu}}, \tag{18a}$$

$$\begin{aligned} 0 < K_P < \frac{1}{\max(\lambda_i)} \Bigg[ & \left( \frac{K_D \max(\lambda_i) \sin(\mu\pi/2)}{\tau} \right)^{\frac{2}{3-\mu}} \\ & - \left( \frac{K_D \max(\lambda_i) \sin(\mu\pi/2)}{\tau} \right)^{\frac{\mu}{3-\mu}} K_D \max(\lambda_i) \cos(\mu\pi/2) \Bigg]. \end{aligned} \tag{18b}$$

For $1 < \mu < 2$:

$$0 < K_D, \tag{19a}$$

$$\begin{aligned} 0 < K_P < \frac{1}{\min(\lambda_i)} \Bigg[ & \left( \frac{K_D \min(\lambda_i) \sin(\mu\pi/2)}{\tau} \right)^{\frac{2}{3-\mu}} \\ & - \left( \frac{K_D \min(\lambda_i) \sin(\mu\pi/2)}{\tau} \right)^{\frac{\mu}{3-\mu}} K_D \min(\lambda_i) \cos(\mu\pi/2) \Bigg]. \end{aligned} \tag{19b}$$

Then the FOPD algorithm guarantees the synchronisation of the speed and acceleration of the followers with that of the leader (i.e., Eqs. (11) and (12) hold). Moreover, the intervehicular distance error between the followers and the leader is:

$$\tilde{s} \to \frac{1}{K_P} V \Lambda^{-1} V^{-1} (\bar{w} - \bar{a}_0). \tag{20}$$

### C. DISTRIBUTED TID CONTROL STRATEGY

In the case of the distributed TID strategy, the follower computes the control action as:

$$\begin{aligned} u_{i\mathrm{TID}}(t) = -\Bigg\{ & \sum_{j=1}^{N} \tilde{a}_{ij} \Bigg( K_T \, {}_0D_t^{-\frac{1}{n}} \left( v_i(t) - v_j(t) \right) \\ & + K_I \left( \int_0^t \left( v_i(\zeta) - v_j(\zeta) \right) d\zeta - d_{ij} \right) \\ & + K_D \left( \frac{d}{dt} \left( v_i(t) - v_j(t) \right) \right) \Bigg) \\ & + p_i \Bigg( K_T \, {}_0D_t^{-\frac{1}{n}} \left( v_i(t) - v_0(t) \right) \\ & + K_I \left( \int_0^t \left( v_i(\zeta) - v_0(\zeta) \right) d\zeta - d_{i0} \right) \\ & + K_D \left( \frac{d}{dt} \left( v_i(t) - v_0(t) \right) \right) \Bigg) \Bigg\}. \end{aligned} \tag{21}$$

The corresponding theorem for the platoon stability with distributed TID can be given:

*Theorem 3 (TID):* Consider a homogeneous platoon of vehicles with $N$ followers, node dynamics given in (2) with the acceleration of the leader and the disturbance vector $\bar{w}$ being constants (either zeros or different from zeros). Assume that the information matrix $\mathcal{H}$ is strictly positive and has real eigenvalues, $n \in (-\infty, -1) \cup (1, \infty)$ and the control gains of the TID strategy are chosen such that the following conditions hold:

$$K_T > 0, \tag{22a}$$

$$K_D > \max_{\lambda_i, i=1,\ldots,N} \left( \frac{\tau \left( \left( \frac{K_T \lambda_i \cos\left(\frac{\pi}{2n}\right)}{\tau} \right)^{\frac{n}{2n+1}} \tan\left(\frac{\pi}{2n}\right) - 1 \right)}{\lambda_i} \right), \tag{22b}$$

$$\begin{aligned} 0 < K_I < \min_{\lambda_i, i=1,\ldots,N} \Bigg( & \left( \frac{K_T \lambda_i \cos\left(\frac{\pi}{2n}\right)}{\tau} \right)^{\frac{2n}{2n+1}} \left( \frac{1}{\lambda_i} + K_D \right) \\ & - \frac{\tau \left( \frac{K_T \lambda_i \cos\left(\frac{\pi}{2n}\right)}{\tau} \right)^{\frac{3n}{2n+1}} \tan\left(\frac{\pi}{2n}\right)}{\lambda_i} \Bigg). \end{aligned} \tag{22c}$$

These conditions hold for $n \in (-\infty, -1) \cup (1, \infty)$. Then the TID algorithm guarantees the synchronisation of the speed and acceleration of the followers with that of the leader (i.e., Eqs. (11) and (12) hold). Moreover, the intervehicular distance error between the followers and the leader is:

$$\tilde{s} \to \frac{1}{K_I} V \Lambda^{-1} V^{-1} (\bar{w} - \bar{a}_0). \tag{23}$$

*Remarks:*

- Both FOPD and the TID strategies are applied to third-order node dynamics, while the FOPID requires that the time lag of the vehicle is negligible; thus, each follower is modelled as a second-order linear system.

- Notice that equations (20) and (23) imply that the FOPD and the TID strategies guarantee the convergence of the intervehicular distances to the desired ones (i.e., also (10) holds) when the acceleration of the leader and the disturbances acting on the follower are zero (i.e., $a_0 = 0$ and $w_i = 0$, with $i = 1, \ldots, N$). This is not a restrictive assumption as it is often required for the synchronisation of the followers' states to that of the leader (see, for instance [12], [18], [67]).
- Different from the FOPD and the TID solutions, the FOPID assures zero intervehicular distance error also for constant leader acceleration and disturbances on the followers.
- As in the case of SISO systems, $n \in (2, 3)$ is a preferable selection for the TID algorithm [33], [68].
- The theorems developed in this paper assume a constant disturbance ($w_i$) applied over the interval $t \in (0, \infty)$ to every follower. However, the simulations are conducted with a constant disturbance applied over the finite interval $t \in (t_1, t_2)$, where $(t_1, t_2) \subset (0, \infty)$. Additionally, this disturbance is applied to a specific follower rather than to all followers, representing a subset of the general case used in the theoretical development. This approach simulates a more realistic platooning scenario, ensuring the latter conditions lie within the subset of the conditions used in the proof.

The proof of Theorems 1-3 presented in Sections IV, V, VI follows the following steps: (i) first, the synchronisation error dynamics are computed; (ii) the closed-loop error dynamics are decomposed and expressed as $N$ independent subsystems; (iii) the range of control parameters guaranteeing asymptotic stability for each subsystem is computed using the root boundary locus (RBL) theory in the Laplace domain; and (iv) the final value theorem is then used to show the convergence of the state errors. In the proof of Theorems 1-3, $u \in \mathbb{R}^N$ is defined as the stack of the control inputs of the $N$ followers, i.e., $u = \begin{bmatrix} u_1 & u_2 & \ldots & u_N \end{bmatrix}^T$.

## V. PROOF OF THEOREM 1

This section deals with the proof of the distributed FOPID controller developed for the two-state node dynamics for the platoon.

### A. CLOSED-LOOP DYNAMICS AND DECOMPOSITION

Consider the node model of the $i$-th vehicle given by equation (1). The position error, velocity error, and acceleration error dynamics of the $i$-th and $j$-th followers can be represented as:

$$\tilde{s}_i(t) = s_i(t) - s_0(t) - d_{i,0}, \tag{24}$$
$$\tilde{s}_j(t) = s_j(t) - s_0(t) - d_{j,0}, \tag{25}$$
$$\tilde{v}_i(t) = v_i(t) - v_0(t), \tag{26}$$
$$\tilde{a}_i(t) = \dot{\tilde{v}}_i(t) = \dot{v}_i(t) - \dot{v}_0(t). \tag{27}$$

Since the leader's acceleration is assumed constant, i.e., $\dot{v}_0(t) = a_0$ (in Theorem 1), then from equation (1) and (27):

$$\dot{\tilde{v}}_i(t) = u_i(t) - a_0 + w_i. \tag{28}$$

Thus:

$$\dot{\tilde{v}}(t) = u(t) - \bar{a}_0 + \bar{w}, \tag{29}$$

with $\bar{a}_0$ and $\bar{w}$ being defined as in (3) and (13), respectively. By using (24)-(25), the control law (15) can be rewritten as:

$$\begin{aligned} u_{i\text{FOPID}}(t) = -\Bigg( & \sum_{j=1}^{N} \tilde{a}_{ij} \Big( K_P(\tilde{s}_i(t) - \tilde{s}_j(t)) \\ & + K_I \int_0^t (\tilde{s}_i(\zeta) - \tilde{s}_j(\zeta)) d\zeta \\ & + K_D \, {}_0D_t^{\mu} (\tilde{s}_i(t) - \tilde{s}_j(t)) \Big) \\ & + p_i \Big( K_P \tilde{s}_i(t) + K_I \int_0^t \tilde{s}_i(\zeta) d\zeta \\ & + K_D \, {}_0D_t^{\mu} \tilde{s}_i(t) \Big) \Bigg). \end{aligned} \tag{30}$$

Furthermore, replacing the adjacency term with the Laplacian matrix, the $i^{\text{th}}$ control action (also shown in [69]) is:

$$\begin{aligned} u_{i\text{FOPID}}(t) = & -K_P(\mathcal{L}\tilde{s}(t))_i - K_I \int_0^t (\mathcal{L}\tilde{s}(\zeta))_i d\zeta \\ & - K_D \, {}_0D_t^{\mu} (L\tilde{s}(t))_i \\ & - K_P p_i \tilde{s}_i(t) - K_I p_i \int_0^t \tilde{s}_i(\zeta) d\zeta \\ & - K_D p_i \, {}_0D_t^{\mu} \tilde{s}_i(t), \end{aligned} \tag{31}$$

where $(\mathcal{L}\tilde{s})_i$ represents the $i$-th entry of the vector $\mathcal{L}\tilde{s}$. Consequently, by considering also (7), the control vector $u$ can be expressed as:

$$u_{\text{FOPID}}(t) = -K_P \mathcal{H} \tilde{s}(t) - K_I \mathcal{H} \int_0^t \tilde{s}(\zeta) d\zeta - K_D \mathcal{H} \, {}_0D_t^{\mu} \tilde{s}(t). \tag{32}$$

Substituting (32) in (29), the platoon closed-loop speed dynamics are:

$$\begin{aligned} \dot{\tilde{v}}(t) = & -K_D \mathcal{H} \tilde{s}(t) - K_I \mathcal{H} \int_0^t \tilde{s}(\zeta) d\zeta \\ & - K_D \mathcal{H} \, {}_0D_t^{\mu} \tilde{s}(t) - \bar{a}_0 + \bar{w}. \end{aligned} \tag{33}$$

Consequently, the closed-loop spacing error between the leader and the followers is:

$$\begin{aligned} \ddot{\tilde{s}}(t) = & -K_P \mathcal{H} \tilde{s}(t) - K_I \mathcal{H} \int_0^t \tilde{s}(\zeta) d\zeta \\ & - K_D \mathcal{H} \, {}_0D_t^{\mu} \tilde{s}(t) - \bar{a}_0 + \bar{w}. \end{aligned} \tag{34}$$

By using the decomposition of the information matrix (8), the dynamics (34) become:

$$\begin{aligned} \ddot{\tilde{s}}(t) = & -K_P V \Lambda V^{-1} \tilde{s}(t) - K_I V \Lambda V^{-1} \int_0^t \tilde{s}(\zeta) d\zeta \\ & - K_D V \Lambda V^{-1} \, {}_0D_t^{\mu} \tilde{s}(t) - \bar{a}_0 + \bar{w}. \end{aligned} \tag{35}$$

Multiplying both sides of (35) by $V^{-1}$:

$$V^{-1}\ddot{\tilde{s}}(t) = -K_P\Lambda V^{-1}\tilde{s}(t) - K_I\Lambda V^{-1}\int_0^t \tilde{s}(\zeta)d\zeta - K_D\Lambda V^{-1}\,{}_0D_t^{\mu}\tilde{s}(t) - V^{-1}\bar{a}_0 + V^{-1}\bar{w}, \quad (36)$$

$$\text{Let } e^{(s)}(t) = V^{-1}\tilde{s}(t), \quad a_t = V^{-1}\bar{a}_0, \quad w_t = V^{-1}\bar{w}. \quad (37)$$

The dynamics of the error $e^{(s)}(t)$ are:

$$\ddot{e}^{(s)}(t) = -K_P\Lambda e^{(s)}(t) - K_I\Lambda\int_0^t e^{(s)}(\zeta)d\zeta - K_D\Lambda\,{}_0D_t^{\mu}e^{(s)}(t) - a_t + w_t. \quad (38)$$

As $\Lambda$ is a diagonal matrix, the equations in (38) are decoupled, and the $e_i$-dynamics are:

$$\ddot{e}_i^{(s)}(t) = -K_P\lambda_i e_i^{(s)}(t) - K_I\lambda_i\int_0^t e_i^{(s)}(\zeta)d\zeta - K_D\lambda_i\,{}_0D_t^{\mu}e_i^{(s)}(t) - a_{ti} + w_{ti}, \quad (39)$$

where $a_{ti}$ and $w_{ti}$ are the $i^{\text{th}}$ entries of $a_t$ and $w_t$, respectively. Consequently, the stability of the platoon system can be ensured by tuning the control gains such that the system in (39) for $i = 1, \ldots, N$ is stable. The evolution of each subsystem in (39) can be studied in the Laplace domain. Specifically, according to [70]: The Laplace transform of the Caputo fractional derivative is given by

$$\mathcal{L}\left\{{}_0D_t^{\mu}e_i^{(s)}(t)\right\} = s^{\mu}E_i^{(s)}(s) - \sum_{k=0}^{\lceil\mu\rceil-1} s^{\mu-k-1}\left(e_i^{(s)}\right)^{(k)}(0), \quad (40)$$

where $\lceil\mu\rceil$ denotes the smallest integer greater than or equal to $\mu$, and $(e_i^{(s)})^{(k)}(0)$ represents the $k$-th derivative at $t = 0$.

Applying the Laplace transform to the system differential equation yields

$$\begin{aligned} s^2E_i^{(s)}(s) - se_i^{(s)}(0) - \dot{e}_i^{(s)}(0) &= -K_P\lambda_iE_i^{(s)}(s) - \frac{K_I\lambda_i}{s}E_i^{(s)}(s) \\ &\quad - K_D\lambda_i\left(s^{\mu}E_i^{(s)}(s) - \sum_{k=0}^{\lceil\mu\rceil-1} s^{\mu-k-1}(e_i^{(s)})^{(k)}(0)\right) \\ &\quad + \frac{w_{ti}-a_{ti}}{s}. \end{aligned} \quad (41)$$

Collecting all terms containing $E_i^{(s)}(s)$ on the left side gives

$$\begin{aligned} E_i^{(s)}(s)\left(s^2 + K_P\lambda_i + \frac{K_I\lambda_i}{s} + K_D\lambda_is^{\mu}\right) &= se_i^{(s)}(0) + \dot{e}_i^{(s)}(0) \\ &\quad + K_D\lambda_i\sum_{k=0}^{\lceil\mu\rceil-1} s^{\mu-k-1}(e_i^{(s)})^{(k)}(0) \\ &\quad + \frac{w_{ti}-a_{ti}}{s}. \end{aligned} \quad (42)$$

Multiplying by $s$ to clear denominators results in

$$\begin{aligned} E_i^{(s)}(s)\left(s^3 + K_P\lambda_is + K_I\lambda_i + K_D\lambda_is^{\mu+1}\right) &= s^2e_i^{(s)}(0) + s\dot{e}_i^{(s)}(0) \\ &\quad + K_D\lambda_i\sum_{k=0}^{\lceil\mu\rceil-1} s^{\mu-k}(e_i^{(s)})^{(k)}(0) \\ &\quad + (w_{ti} - a_{ti}). \end{aligned} \quad (43)$$

Solving for $E_i^{(s)}(s)$ yields the general solution

$$E_i^{(s)}(s) = \frac{s^2e_i^{(s)}(0) + s\dot{e}_i^{(s)}(0)}{M(s)} + \frac{K_D\lambda_i\sum_{k=0}^{\lceil\mu\rceil-1} s^{\mu-k}(e_i^{(s)})^{(k)}(0)}{M(s)} + \frac{w_{ti}-a_{ti}}{M(s)}, \quad (44)$$

where the characteristic polynomial is defined as

$$M(s) = s^3 + K_D\lambda_is^{\mu+1} + K_P\lambda_is + K_I\lambda_i. \quad (45)$$

The summation term in (44) can be expanded for specific ranges of $\mu$.

*Case 1:* For $0 < \mu \leq 1$, where $\lceil\mu\rceil = 1$, the summation reduces to a single term with $k = 0$:

$$E_i^{(s)}(s) = \frac{s^2e_i^{(s)}(0) + s\dot{e}_i^{(s)}(0) + K_D\lambda_is^{\mu}e_i^{(s)}(0)}{M(s)} + \frac{w_{ti}-a_{ti}}{M(s)}. \quad (46)$$

*Case 2:* For $1 < \mu \leq 2$, where $\lceil\mu\rceil = 2$, the summation contains two terms ($k = 0$ and $k = 1$):

$$E_i^{(s)}(s) = \frac{s^2e_i^{(s)}(0) + s\dot{e}_i^{(s)}(0)}{M(s)} + \frac{K_D\lambda_i\left(s^{\mu}e_i^{(s)}(0) + s^{\mu-1}\dot{e}_i^{(s)}(0)\right)}{M(s)} + \frac{w_{ti}-a_{ti}}{M(s)}. \quad (47)$$

The stability analysis for both cases relies on the same characteristic equation given in (45).

### B. STABILITY ANALYSIS

The stability analysis for the characteristic equation (45) is carried out using the root boundary locus approach, as reviewed in Appendix B. The real root boundary (RRB) is found when $M(s) = 0$ at $s = 0$, thus:

$$s^3 + K_D\lambda_is^{\mu+1} + K_P\lambda_is + K_I\lambda_i = 0 \quad \Rightarrow \quad K_I = 0. \quad (48)$$

To find the complex root boundary (CRB), substitute $s = j\omega$ into $M(s)$, and find conditions for $\Re\{M(j\omega)\} = 0$ and $\Im\{M(j\omega)\} = 0$. When $s = j\omega$ in (45), $M(j\omega) = 0$ becomes:

$$(j\omega)^3 + K_D\lambda_i(j\omega)^{\mu+1} + (j\omega)K_P\lambda_i + K_I\lambda_i = 0. \quad (49)$$

By using Euler's formula for complex numbers, it can be rewritten as:

$$-j\omega^3+K_D\lambda_i\omega^{\mu+1}\left(\cos\left((\mu+1)\frac{\pi}{2}\right)+j\sin\left((\mu+1)\frac{\pi}{2}\right)\right)+j\omega K_P\lambda_i+K_I\lambda_i=0. \tag{50}$$

Consequently, by separating the real part and the imaginary part and imposing $\Re\{M(j\omega)\}=0$ and $\Im\{M(j\omega)\}=0$, the following equations are obtained:

$$\Re\{M(j\omega)\}=-K_D\lambda_i\omega^{\mu+1}\sin\left(\mu\frac{\pi}{2}\right)+K_I\lambda_i=0, \tag{51}$$

$$\implies K_I=K_D\omega^{\mu+1}\sin\left(\mu\frac{\pi}{2}\right), \tag{52}$$

$$\Im\{M(j\omega)\}=-\omega^3+K_D\lambda_i\omega^{\mu+1}\cos\left(\mu\frac{\pi}{2}\right)+\omega K_P\lambda_i=0, \tag{53}$$

$$\implies K_P=\frac{\omega^2}{\lambda_i}-K_D\omega^{\mu}\cos\left(\mu\frac{\pi}{2}\right). \tag{54}$$

The non-parametric equations above provide the values of $K_I$ and $K_P$ for which equation (49) has a pair of complex roots in position $\pm j\omega$. From equation (52), we have:

$$\omega=\left(\frac{K_I}{K_D\sin\left(\mu\frac{\pi}{2}\right)}\right)^{\frac{1}{\mu+1}}. \tag{55}$$

By replacing equation (55) in equation (54), we obtain:

$$K_P=\frac{1}{\lambda_i}\left(\frac{K_I}{K_D\sin\left(\mu\frac{\pi}{2}\right)}\right)^{\frac{2}{\mu+1}}-K_D\left(\frac{K_I}{K_D\sin\left(\mu\frac{\pi}{2}\right)}\right)^{\frac{\mu}{\mu+1}}\cos\left(\mu\frac{\pi}{2}\right). \tag{56}$$

This provides the relationship among the control gains for having imaginary roots for the characteristic equation (45). For any $K_D$, equation (56) divides the parameter space $(K_I, K_P)$ into two regions. According to Appendix B, for determining the stability region, the sign of the determinant of the Jacobian $\tilde{J}$ should be evaluated. From the equations (51) and (53):

$$\tilde{J}=\begin{bmatrix}\frac{\partial\Re\{M(j\omega)\}}{\partial K_I} & \frac{\partial\Re\{M(j\omega)\}}{\partial K_P}\\ \frac{\partial\Im\{M(j\omega)\}}{\partial K_I} & \frac{\partial\Im\{M(j\omega)\}}{\partial K_P}\end{bmatrix}=\begin{bmatrix}\lambda_i & 0\\ 0 & \omega\lambda_i\end{bmatrix}. \tag{57}$$

Hence, the determinant of $\tilde{J}$ is:

$$\det(\tilde{J})=\omega\lambda_i^2. \tag{58}$$

Since $\det(\tilde{J})>0$ for any $\omega>0$, the stability region lies on the left-hand side of the CRB curve in the $K_I-K_P$ plane, in the direction of increasing $\omega$ when curve (56) is plotted. This stability condition can be expressed as a non-parametric equation that defines the parameter space $(K_I, K_P)$, ensuring the system remains stable. Considering the smallest eigenvalue $\min(\lambda_i)$ for the distributed system, the overall stability of the platoon system is given by:

$$K_P>\frac{\left(\frac{K_I}{K_D\sin(\mu\frac{\pi}{2})}\right)^{\frac{2}{\mu+1}}}{\min(\lambda_i)}-K_D\left(\frac{K_I}{K_D\sin\left(\mu\frac{\pi}{2}\right)}\right)^{\frac{\mu}{\mu+1}}\cos\left(\mu\frac{\pi}{2}\right), \tag{59}$$

$$K_I>0. \tag{60}$$

### C. CONVERGENCE OF STATES

When the subsystems in (38) are stable, the final value theorem (explained in [71]) can be used to determine the steady-state value of the errors, i.e.,

$$\lim_{t\to\infty}e_i^{(s)}(t)=\lim_{s\to0}sE_i^{(s)}(s). \tag{61}$$

By using (46) and (47), it follows that $sE_i^{(s)}(s)\to0$ as $s\to0$. Thus:

$$\lim_{t\to\infty}e^{(s)}(t)=0. \tag{62}$$

Equation (62) implies that the intervehicular distance between the follower and that of the leader becomes the desired intervehicular distance asymptotically. Since $e^{(s)}(t)=V^{-1}\tilde{s}(t)$ then:

$$\lim_{t\to\infty}\tilde{s}(t)=\lim_{t\to\infty}Ve^{(s)}(t)=0. \tag{63}$$

Differentiating the position error in (63), the velocity error equation at time tending to infinity becomes:

$$\lim_{t\to\infty}\dot{\tilde{v}}(t)=\lim_{t\to\infty}\frac{d}{dt}\tilde{s}(t)=\lim_{t\to\infty}\frac{d}{dt}Ve^{(s)}(t)=\lim_{s\to0}s^2E^{(s)}(s)=0, \tag{64}$$

where, $E^{(s)}(s)=\left[E_1^{(s)}(s)\ E_2^{(s)}(s)\ \dots\ E_N^{(s)}(s)\right]^\top$. Hence, the velocity of the followers reaches consensus with the velocity of the leader as time tends to infinity.

## VI. PROOF OF THEOREM 2

This section deals with the proof of the distributed FOPD controller developed when the followers are modelled with third-order systems (2). The proof follows the same steps presented for Theorem 1.

### A. CLOSED-LOOP DYNAMICS AND DECOMPOSITION

By considering the control action in (17) and following a similar process as in Section V, the control vector is:

$$u_{\text{FOPD}}(t)=-K_P\mathcal{H}\tilde{s}(t)-K_D\mathcal{H}\,{}_0D_t^{\mu}\tilde{s}(t). \tag{65}$$

Consequently, the closed-loop system, when the follower dynamics are given by (2), is:

$$\ddot{\tilde{v}}(t)=-\frac{1}{\tau}\left(\dot{\tilde{v}}(t)+\bar{a}_0\right)+\frac{1}{\tau}\left(-K_P\mathcal{H}\tilde{s}(t)-K_D\mathcal{H}\,{}_0D_t^{\mu}\tilde{s}(t)\right)+\frac{1}{\tau}\bar{w}. \tag{66}$$

Hence, the closed-loop velocity error dynamics between the leader and the followers are:

$$\dot{\tilde{v}}(t) = -\frac{1}{\tau}\left(\tilde{v}(t) + \bar{a}_0\right) + \frac{1}{\tau}\left(-K_P\,\mathcal{H}\int_0^t \tilde{v}(\zeta)\,d\zeta - K_D\,\mathcal{H}\,{}_0D_t^{\mu-1}\tilde{v}(t)\right) + \frac{1}{\tau}\bar{w}. \tag{67}$$

Applying decomposition of the information matrix (8), and multiplying by $V^{-1}$ both side, equation (67) then becomes:

$$V^{-1}\dot{\tilde{v}}(t) = -\frac{1}{\tau}\left(V^{-1}\tilde{v}(t) + V^{-1}\bar{a}_0\right) + \frac{1}{\tau}\left(-K_P\,\Lambda\,V^{-1}\int_0^t \tilde{v}(\zeta)\,d\zeta - K_D\,\Lambda\,V^{-1}\,{}_0D_t^{\mu-1}\tilde{v}(t)\right) + \frac{1}{\tau}V^{-1}\bar{w}. \tag{68}$$

Let $e^{(v)}(t) = V^{-1}\tilde{v}(t)$. Then, the dynamics of the error $e^{(v)}(t)$ are given by:

$$\dot{e}^{(v)}(t) = -\frac{1}{\tau}\left(e^{(v)}(t) + a_t\right) + \frac{1}{\tau}\left(-K_P\,\mathcal{H}\int_0^t e^{(v)}(\zeta)\,d\zeta - K_D\,\mathcal{H}\,{}_0D_t^{\mu-1}e^{(v)}(t)\right) + \frac{1}{\tau}w_t\,, \tag{69}$$

where $a_t$ and $w_t$, are defined in (37). After decoupling (69), the $e_i^{(v)}$ dynamics are:

$$rCl\dot{e}_i^{(v)}(t) = -\frac{1}{\tau}\left(e_i^{(v)}(t) + a_{t_i}\right) + \frac{1}{\tau}\left(-K_P\,\lambda_i\int_0^t e_i^{(v)}(\zeta)\,d\zeta - K_D\,\lambda_i\,{}_0D_t^{\mu-1}e_i^{(v)}(t)\right) + \frac{1}{\tau}w_{t_i}\,. \tag{70}$$

By applying the Laplace transform to equation (70) becomes:‘‘‘latex

$$\begin{aligned} s^2E_i^{(v)}(s) - s\,e_i^{(v)}(0) - \dot{e}_i^{(v)}(0) &= -\tau^{-1}\left(sE_i^{(v)}(s) - e_i^{(v)}(0)\right) - \tau^{-1}\frac{a_{t_i}}{s} \\ &\quad + \tau^{-1}\left(-K_P\,\lambda_i\frac{E_i^{(v)}(s)}{s} - K_D\,\lambda_i\,s^{\mu-1}E_i^{(v)}(s) + K_D\,\lambda_i\sum_{k=0}^{\lceil\mu\rceil-1}s^{\mu-2-k}(e_i^{(v)})^{(k)}(0)\right) + \frac{w_{t_i}}{\tau\,s}. \end{aligned} \tag{71}$$

Thus, the $i^{\text{th}}$ error is described in the Laplace domain as:

$$E_i^{(v)}(s) = \frac{\tau s^2e_i^{(v)}(0) + \tau s\dot{e}_i^{(v)}(0) + s\,e_i^{(v)}(0) - a_{t_i} + w_{t_i}}{\tau s^3 + s^2 + K_D\lambda_i s^\mu + K_P\lambda_i} + \frac{K_D\lambda_i\sum_{k=0}^{\lceil\mu\rceil-1}s^{\mu-1-k}\left(e_i^{(v)}\right)^{(k)}(0)}{\tau s^3 + s^2 + K_D\lambda_i s^\mu + K_P\lambda_i}. \tag{72}$$

Therefore, when $0 < \mu \le 1$:

$$E_i^{(v)}(s) = \frac{\tau s^2e_i^{(v)}(0) + \tau s\dot{e}_i^{(v)}(0) + s\,e_i^{(v)}(0) - a_{t_i} + w_{t_i}}{\tau s^3 + s^2 + K_D\lambda_i s^\mu + K_P\lambda_i} + \frac{K_D\lambda_i\,s^{\mu-1}e_i^{(v)}(0)}{\tau s^3 + s^2 + K_D\lambda_i s^\mu + K_P\lambda_i}. \tag{73}$$

While for $1 < \mu \le 2$:

$$E_i^{(v)}(s) = \frac{\tau s^2e_i^{(v)}(0) + \tau s\dot{e}_i^{(v)}(0) + s\,e_i^{(v)}(0) - a_{t_i} + w_{t_i}}{\tau s^3 + s^2 + K_D\lambda_i s^\mu + K_P\lambda_i} + \frac{K_D\lambda_i\left(s^{\mu-1}e_i^{(v)}(0) + s^{\mu-2}\dot{e}_i^{(v)}(0)\right)}{\tau s^3 + s^2 + K_D\lambda_i s^\mu + K_P\lambda_i}. \tag{74}$$

Hence, the convergence of the errors in (73) and (74) depends on the characteristic polynomial:

$$M(s) = \tau s^3 + s^2 + K_D\lambda_i s^\mu + K_P\lambda_i. \tag{75}$$

### B. STABILITY ANALYSIS

For the characteristic equation (75), the RRB is $K_P = 0$. The complex root boundary (CRB) is given by:

$$-\tau j\omega^3 - \omega^2 + K_P\lambda_i + K_D\lambda_i\omega^\mu\left(\cos\left(\mu\frac{\pi}{2}\right) + j\sin\left(\mu\frac{\pi}{2}\right)\right) = 0. \tag{76}$$

Separating real and imaginary parts:

$$\Re\{M(j\omega)\} = -\omega^2 + \omega^\mu K_D\lambda_i\cos\left(\mu\frac{\pi}{2}\right) + K_P\lambda_i = 0, \tag{77}$$

$$\Im\{M(j\omega)\} = -\tau\omega^3 + \omega^\mu K_D\lambda_i\sin\left(\mu\frac{\pi}{2}\right) = 0. \tag{78}$$

By solving (78) for $\omega$ and substituting into (77), the non-parametric stability equation is obtained as:

$$K_P = \frac{1}{\lambda_i}\left[\left(\frac{K_D\lambda_i\sin\left(\mu\frac{\pi}{2}\right)}{\tau}\right)^{\frac{2}{3-\mu}} - \left(\frac{K_D\lambda_i\sin\left(\mu\frac{\pi}{2}\right)}{\tau}\right)^{\frac{\mu}{3-\mu}} K_D\lambda_i\cos\left(\mu\frac{\pi}{2}\right)\right]. \tag{79}$$

The equation (79) divides the parameter space $(K_D, K_P)$ into in two regions. The region of the parameter space which guarantees stability can be found by studying the Jacobian. The Jacobian matrix $\tilde{J}$ is expressed as:

$$\tilde{J} = \begin{bmatrix} \frac{\partial\Re\{M(j\omega)\}}{\partial K_D} & \frac{\partial\Re\{M(j\omega)\}}{\partial K_P} \\ \frac{\partial\Im\{M(j\omega)\}}{\partial K_D} & \frac{\partial\Im\{M(j\omega)\}}{\partial K_P} \end{bmatrix} = \begin{bmatrix} \omega^\mu\lambda_i\sin(\mu\pi/2) & \lambda_i \\ \omega^\mu\lambda_i\sin(\mu\pi/2) & 0 \end{bmatrix}. \tag{80}$$

The determinant of $\tilde{J}$ is:

$$\det(\tilde{J}) = -\omega^\mu\lambda_i^2\sin(\mu\pi/2). \tag{81}$$

Since $\det(\tilde{J}) < 0$ for any $\omega > 0$ and $0 < \mu < 2$, the stability region lies on the right-hand side of the CRB curve given by (81) in the $K_P$-$K_D$ plane in the direction of increasing $\omega$.

Hence, the $i$th subsystem is stable when:

$$0 < K_P < \frac{1}{\lambda_i}\left[\left(\frac{K_D\lambda_i \sin(\mu\pi/2)}{\tau}\right)^{\frac{2}{3-\mu}} - \left(\frac{K_D\lambda_i \sin(\mu\pi/2)}{\tau}\right)^{\frac{\mu}{3-\mu}} K_D\lambda_i \cos(\mu\pi/2)\right]. \quad (82)$$

Equation (82) can be satisfied when the right-hand side is strictly positive. This requires conditions on the $K_D$ control gain. Specifically: - For $1 < \mu < 2$, the terms on the right-hand side of (82) are positive for any $K_D > 0$ and for any value of $\tau$ or $\lambda_i$. - For $0 < \mu < 1$, the first term remains positive, but the second term becomes negative. In this case, the right-hand side is strictly positive when:

$$K_D < \frac{\sin^{2-\mu}(\mu\pi/2)}{\tau^{2-\mu}\lambda_i \cos^{3-\mu}(\mu\pi/2)}. \quad (83)$$

To fulfill condition (83) for all subsystems, $K_D$ must satisfy:

$$K_D < \frac{\sin^{2-\mu}(\mu\pi/2)}{\tau^{2-\mu}\max(\lambda_i)\cos^{3-\mu}(\mu\pi/2)}, \quad 0 < \mu < 1. \quad (84)$$

Now investigating the nature of the stability function with respect to $\lambda_i$ for equation (84): Let

$$A = \left(\frac{K_D \sin(\mu\pi/2)}{\tau}\right)^{\frac{1}{3-\mu}}; \quad \alpha = \cos(\mu\pi/2), \quad (85)$$

then:

$$K_P = A^2\lambda_i^{\frac{\mu-1}{3-\mu}} - A^\mu K_D\alpha\lambda_i^{\frac{\mu}{3-\mu}}. \quad (86)$$

Taking the derivative of $K_P$ with respect to $\lambda_i$:

$$\frac{dK_P}{d\lambda_i} = A^2\frac{\mu-1}{3-\mu}\lambda_i^{\frac{2\mu-4}{3-\mu}} - A^\mu K_D\alpha\frac{\mu}{3-\mu}\lambda_i^{\frac{2\mu-3}{3-\mu}}. \quad (87)$$

For $0 < \mu < 1$:

$$\frac{dK_P}{d\lambda_i} < 0, \quad (88)$$

indicating that $\lambda_{\max}$ is the relevant value. Thus:

$$0 < K_P < \frac{1}{\max(\lambda_i)}\left[\left(\frac{K_D\max(\lambda_i)\sin(\mu\pi/2)}{\tau}\right)^{\frac{2}{3-\mu}} - \left(\frac{K_D\max(\lambda_i)\sin(\mu\pi/2)}{\tau}\right)^{\frac{\mu}{3-\mu}} K_D\max(\lambda_i)\cos(\mu\pi/2)\right]. \quad (89)$$

For $1 < \mu < 2$:

$$\frac{dK_P}{d\lambda_i} > 0, \quad (90)$$

indicating that $\lambda_{\min}$ is the relevant value. Thus:

$$0 < K_P < \frac{1}{\min(\lambda_i)}\left[\left(\frac{K_D\min(\lambda_i)\sin(\mu\pi/2)}{\tau}\right)^{\frac{2}{3-\mu}} - \left(\frac{K_D\min(\lambda_i)\sin(\mu\pi/2)}{\tau}\right)^{\frac{\mu}{3-\mu}} K_D\min(\lambda_i)\cos(\mu\pi/2)\right]. \quad (91)$$

*Condition on $K_D$:* The stability condition (82) must hold only if equation (82) yields real and positive values for $K_P$. Hence, to ensure $K_P$ remains positive, the following inequalities should be followed for different ranges of $\mu$:

$$0 < \mu < 1,\ 0 < K_D < \frac{\sin^{2-\mu}(\mu\pi/2)}{\tau^{2-\mu}\times\max(\lambda_i)\times\cos^{3-\mu}(\mu\pi/2)}, \quad (92)$$

$$1 < \mu < 2,\ K_D > 0. \quad (93)$$

### C. CONVERGENCE AND RESIDUAL ERROR

Similar to equation (69), $e^{(s)}(t) = V^{-1}\tilde{s}(t)$, the dynamics of the position error for the $i^{\text{th}}$ subsystem is:

$$\ddot{e}_i^{(s)}(t) = -\frac{1}{\tau}\left(\ddot{e}_i^{(s)}(t) + a_{t_i}\right) + \frac{1}{\tau}\left(-K_P\lambda_i e_i^{(s)}(t) - K_D\lambda_i\, {}_0D_t^\mu e_i^{(s)}(t)\right) + \frac{w_{t_i}}{\tau}. \quad (94)$$

By applying the Laplace transform to both sides of (94) and after algebraic manipulations, the expression of $E_i^{(s)}(s)$ is:

$$E_i^{(s)}(s) = \frac{\tau s^3 e_i^{(s)}(0) + \tau s^2\dot{e}_i^{(s)}(0) + \tau s\ddot{e}_i^{(s)}(0) - a_{t_i}}{s\left(\tau s^3 + s^2 + K_P\lambda_i + K_D\lambda_i s^\mu\right)} + \frac{s^2 e_i^{(s)}(0) + s\dot{e}_i^{(s)}(0) + K_D\lambda_i\sum_{k=0}^{\lceil\mu\rceil-1} s^{\mu-k}(e_i^{(s)})^{(k)}(0) + w_{t_i}}{s\left(\tau s^3 + s^2 + K_P\lambda_i + K_D\lambda_i s^\mu\right)}. \quad (95)$$

Consequently, by considering (61), the final value theorem implies:

$$\lim_{t\to\infty} e_i^{(s)}(t) = \lim_{s\to 0} sE_i^{(s)}(s) = \frac{w_{t,i} - a_{t,i}}{K_P\lambda_i}, \quad i = 1, 2, \ldots, N. \quad (96)$$

Hence, from (37):

$$\lim_{t\to\infty}\tilde{s}(t) = \lim_{t\to\infty} e^{(s)}(t) = \frac{V}{K_P}\Lambda^{-1}\left(V^{-1}\bar{w} - V^{-1}\bar{a}_0\right) = \frac{V}{K_P}\Lambda^{-1}V^{-1}\left(\bar{w} - \bar{a}_0\right). \quad (97)$$

Hence, if there are no disturbances and the acceleration of the leader is zero, the $\lim_{t\to\infty}\tilde{s}(t) = 0$ (i.e., the required intervehicular distance is imposed). Furthermore, by defining $E^{(s)}(s) = [E_1^{(s)}(s), E_2^{(s)}(s), \ldots, E_N^{(s)}(s)]^T$, also implies:

$$\lim_{t\to\infty}\dot{\tilde{v}}(t) = \lim_{t\to\infty}\frac{d}{dt}\tilde{s}(t) = \lim_{t\to\infty}\frac{d}{dt}Ve^{(s)}(t) = V\lim_{s\to 0} s^2E^{(s)}(s) = 0. \quad (98)$$

Similarly:

$$\lim_{t\to\infty}\ddot{\tilde{v}}(t) = \lim_{t\to\infty}\frac{d^2}{dt^2}\tilde{s}(t) = \lim_{t\to\infty}\frac{d^2}{dt^2}Ve^{(s)}(t)$$

$$= V \lim_{s\to 0} s^3 E^{(s)}(s) = 0. \tag{99}$$

Hence, the velocity and acceleration of the followers reach asymptotically consensus with the velocity and acceleration also in the presence of residual position errors, and thus Theorem 2 remains proven.

## VII. PROOF OF THEOREM 3

### A. CLOSED-LOOP DYNAMICS AND DECOMPOSITION

By considering the control action in (21) and following similar steps presented in Section V, the control vector is:

$$u_{\text{TID}}(t) = -K_T \mathcal{H} D^{-1/n} \tilde{v}(t) - K_I \mathcal{H}\Big(\int_0^t \tilde{v}(\zeta) d\zeta + \bar{d}\Big) - K_D \mathcal{H} \dot{\tilde{v}}(t), \tag{100}$$

where $\bar{d}$ is the vector of intervehicular distances with the leader and the followers respectively, i.e., $[d_{10}, d_{20}, \ldots, d_{N0}]^T$. Assuming the leader's acceleration is constant, the lumped dynamics for the entire platoon become:

$$\ddot{\tilde{v}}(t) = -\frac{1}{\tau}\big(\dot{\tilde{v}}(t) + \bar{a}_0\big) + \frac{1}{\tau}\Big(-K_T\, \mathcal{H}\, D^{-1/n} \tilde{v}(t) - K_I\, \mathcal{H}\big(\int_0^t \tilde{v}(\zeta)\, d\zeta + \bar{d}\big) - K_D\, \mathcal{H}\, \dot{\tilde{v}}(t)\Big) + \frac{\bar{w}}{\tau}. \tag{101}$$

By defining $e^{(v)}(t) = V^{-1}\tilde{v}(t)$; $d_f = V^{-1}\bar{d}$ and by using the steps carried out in (67)-(69). The dynamics of the $i^{\text{th}}$ error $e_i^{(v)}$ are:

$$\ddot{e}_i^{(v)}(t) = -\frac{1}{\tau}\big(\dot{e}_i^{(v)}(t) + a_{t_i}\big) + \frac{1}{\tau}\Big(-K_T\, \lambda_i\, D^{-1/n} e_i^{(v)}(t) - K_I\, \lambda_i \big(\int_0^t e_i^{(v)}(\zeta)\, d\zeta + d_{f_i}\big) - K_D\, \lambda_i\, \dot{e}_i^{(v)}(t)\Big) + \frac{w_{t_i}}{\tau}, \tag{102}$$

where $a_{ti}$ and $w_{ti}$ are defined in (37). By taking the Laplace transform of both sides of (102), the expression for the Laplace transform of $e_i^{(v)}(t)$ can be derived as:

$$E_i^{(v)}(s) = \frac{\tau s^2 e_i^{(v)}(0) + \tau s \dot{e}_i^{(v)}(0)}{\tau s^3 + (1 + K_D\lambda_i)s^2 + K_T\lambda_i s^{1-1/n} + K_I\lambda_i} + \frac{(1 + K_D\lambda_i)s e_i^{(v)}(0) - a_{ti} - K_I\lambda_i d_{fi} + w_{ti}}{\tau s^3 + (1 + K_D\lambda_i)s^2 + K_T\lambda_i s^{1-1/n} + K_I\lambda_i}. \tag{103}$$

The characteristic polynomial for studying the closed-loop stability is:

$$M(s) = \tau s^3 + (1 + K_D\lambda_i)s^2 + K_T\lambda_i s^{1-1/n} + K_I\lambda_i. \tag{104}$$

### B. STABILITY ANALYSIS

For equation (104), the RRB is:

$$\tau s^3 + (1 + K_D\lambda_i)s^2 + K_T\lambda_i s^{1-1/n} + K_I\lambda_i\Big|_{s=0} \implies K_I = 0. \tag{105}$$

Moreover, the real part and the imaginary part of $M(j\omega)$ are set to zero to obtain the CRB, thus having:

$$\Re\{M(j\omega)\} = -(1 + K_D\lambda_i)\omega^2 + \lambda_i K_T \omega^{1-1/n} \sin\Big(\frac{\pi}{2n}\Big) + \lambda_i K_I = 0, \tag{106}$$

$$\Im\{M(j\omega)\} = -\tau\omega^3 + \lambda_i K_T \omega^{1-1/n} \cos\Big(\frac{\pi}{2n}\Big) = 0. \tag{107}$$

Hence, the curve describing in the parameter space $(K_T, K_I)$ the locus where $M(j\omega)$ has poles crossing the imaginary axis is:

$$K_T = \frac{\tau\omega^{2+1/n}}{\lambda_i \cos\left(\frac{\pi}{2n}\right)}, \tag{108}$$

$$K_I = \omega^2\left(\frac{1}{\lambda_i} + K_D\right) - \frac{\tau\omega^3}{\lambda_i}\tan\Big(\frac{\pi}{2n}\Big). \tag{109}$$

From equation (108), $\omega$ can be computed as:

$$\omega = \left(\frac{K_T\lambda_i \cos\left(\frac{\pi}{2n}\right)}{\tau}\right)^{\frac{n}{2n+1}}, \tag{110}$$

and thus, by substituting (110) into (109), the non-parametric equation describing the curve dividing the stable region from the unstable one is:

$$K_I = \left(\frac{1}{\lambda_i} + K_D\right)\left(\frac{K_T\lambda_i \cos\left(\frac{\pi}{2n}\right)}{\tau}\right)^{\frac{2n}{2n+1}} - \frac{\tau}{\lambda_i}\left(\frac{K_T\lambda_i \cos\left(\frac{\pi}{2n}\right)}{\tau}\right)^{\frac{3n}{2n+1}} \tan\Big(\frac{\pi}{2n}\Big). \tag{111}$$

The equation (111) divides the parameter space $(K_I, K_T)$ into two regions. The region guaranteeing stability of the $i^{\text{th}}$ subsystem (102) can be determined by analysing the sign of the Jacobian matrix $\tilde{J}$:

$$\tilde{J} = \begin{bmatrix} \frac{\partial \text{Re}\{M(j\omega)\}}{\partial K_T} & \frac{\partial \text{Re}\{M(j\omega)\}}{\partial K_I} \\ \frac{\partial \text{Im}\{M(j\omega)\}}{\partial K_T} & \frac{\partial \text{Im}\{M(j\omega)\}}{\partial K_I} \end{bmatrix} = \begin{bmatrix} \lambda_i\omega^{1-\frac{1}{n}} \sin\left(\frac{\pi}{2n}\right) & \lambda_i \\ \lambda_i\omega^{1-\frac{1}{n}} \cos\left(\frac{\pi}{2n}\right) & 0 \end{bmatrix}. \tag{112}$$

Hence, the determinant of $\tilde{J}$ is:

$$\det(\tilde{J}) = -\lambda_i^2\omega^{1-\frac{1}{n}} \cos\Big(\frac{\pi}{2n}\Big). \tag{113}$$

The sign of $\det(\tilde{J})$ depends on the value of $n$, and four cases are possible:

- If $n > 1$ or $n < -1$, then $\cos\left(\frac{\pi}{2n}\right) > 0$, and $\det(\tilde{J}) < 0$. Hence, the stable region is on the right of the curve $(K_T(\omega), K_I(\omega))$.
- If $n = \pm 1$, then $\cos\left(\frac{\pi}{2n}\right) = 0$, and the criterion cannot be applied.

Since $\det(\tilde{J}) < 0$ for any $\omega > 0$ when $n > 1$ or $n < -1$, the stability region is on the right-hand side of the CRB curve in the $K_T$-$K_I$ plane. Hence, the stability condition for

the $i^{\text{th}}$ subsystem, when the non-parametric equation (111) is considered, is:

$$0 < K_I < \left(\frac{K_T\lambda_i\cos\left(\frac{\pi}{2n}\right)}{\tau}\right)^{\frac{2n}{2n+1}}\left(\frac{1}{\lambda_i}+K_D\right) - \frac{\tau}{\lambda_i}\left(\frac{K_T\lambda_i\cos\left(\frac{\pi}{2n}\right)}{\tau}\right)^{\frac{3n}{2n+1}}\tan\left(\frac{\pi}{2n}\right) \quad n\in(-\infty,-1)\cup(1,\infty). \tag{114}$$

To avoid an empty set on the right side of (114), thus making the inequality infeasible, the following conditions on $K_T$ and $K_I$ are imposed. Specifically, to guarantee the right side of (114) is real, it is required that $K_T^{\frac{2n}{2n+1}}$ is real, which is obtained by imposing $K_T \geq 0$. Moreover, the right side of (114) is positive when the first term is greater than the second, which can be obtained by imposing:

$$K_D > \frac{\tau\left(\frac{K_T\lambda_i\cos\left(\frac{\pi}{2n}\right)}{\tau}\right)^{\frac{n}{2n+1}}\tan\left(\frac{\pi}{2n}\right)-1}{\lambda_i}. \tag{115}$$

Equation (115) is satisfied for all $N$ characteristic equations (104) when:

$$K_D > \max\left\{\frac{\tau\left(\frac{K_T\lambda_i\cos\left(\frac{\pi}{2n}\right)}{\tau}\right)^{\frac{n}{2n+1}}\tan\left(\frac{\pi}{2n}\right)-1}{\lambda_i}\right\}_{i=1,\ldots,N}. \tag{116}$$

By guaranteeing that the right-hand side of (114) is positive for each subsystem, the platoon stability is obtained by imposing:

$$0 < K_I < \min\left\{\left(\frac{K_T\lambda_i\cos\left(\frac{\pi}{2n}\right)}{\tau}\right)^{\frac{2n}{2n+1}}\left(\frac{1}{\lambda_i}+K_D\right) - \frac{\tau}{\lambda_i}\left(\frac{K_T\lambda_i\cos\left(\frac{\pi}{2n}\right)}{\tau}\right)^{\frac{3n}{2n+1}}\tan\left(\frac{\pi}{2n}\right)\right\}_{i=1,\ldots,N} \quad n\in(-\infty,-1)\cup(1,\infty), \tag{117}$$

which assures that (116) is fulfilled for all subsystems of (102).

### C. CONVERGENCE OF STATES

By defining $e^{(s)}(t) = V^{-1}\tilde{s}(t)$ and following the steps detailed in Section VI, the spacing error in the Laplace domain for the $i^{\text{th}}$ subsystem is:

$$E_i^{(s)}(s) = \frac{\tau s^3 e_i^{(s)}(0) + s^2\left[\tau\dot{e}_i^{(s)}(0) + e_i^{(s)}(0) + K_D\lambda_i\, e_i^{(s)}(0)\right]}{\tau s^3 + (1+K_D\lambda_i)s^2 + K_T\lambda_i s^{1-1/n} + K_I\lambda_i} + \frac{s\left[\tau\ddot{e}_i^{(s)}(0) + \dot{e}_i^{(s)}(0) + K_D\lambda_i\,\dot{e}_i^{(s)}(0)\right] - a_{ti} + w_{ti}}{\tau s^3 + (1+K_D\lambda_i)s^2 + K_T\lambda_i s^{1-1/n} + K_I\lambda_i}. \tag{118}$$

Using the final value theorem, the asymptotic spacing error is:

$$\lim_{t\to\infty} e_i^{(s)}(t) = \frac{w_{ti}-a_{ti}}{K_I\lambda_i}. \tag{119}$$

Similarly, the velocity and acceleration errors converge to zero as:

$$\lim_{t\to\infty}\dot{\tilde{v}}(t) = 0, \tag{120}$$

$$\lim_{t\to\infty}\ddot{\tilde{v}}(t) = 0. \tag{121}$$

Thus, Theorem 3 is proven.

## VIII. SIMULATION ANALYSIS

This section presents three simulation analysis. Firstly, it is shown numerically that Theorems 1, 2, and 3 can be effectively used for finding the stability region of the control parameters. Furthermore, the impact of including and excluding external disturbances is also examined. The second simulation campaign aims to test the closed-loop tracking performance for a realistic speed profile, i.e., when the leader's speed profile is the Worldwide Harmonised Light Vehicles Test Procedure (WLTP) manoeuvre [72]. This scenario, composed of four distinct sub-manoeuvres, is utilised to assess performance across different platoon lengths. The closed-loop tracking performance of the novel fractional-order control solutions is compared against their corresponding integer-order counterparts. Performance is quantitatively evaluated by considering the maximum tracking error observed during each sub-manoeuvre. Finally, a robustness analysis is carried out. This simulation analysis extends to a heterogeneous platoon where vehicles are characterised by nonlinear node dynamics, having different model parameters and considering model uncertainties.

### A. NUMERICAL VALIDATION OF THE MAIN THEOREMS

To validate Theorems 1, 2, and 3, a platoon comprising four follower vehicles is simulated. A constant intravehicular distance of 20 m is maintained, while the leader's speed is held constant at 20 m/s. For the FOPD and TID strategies, the node dynamics incorporate a time-lag $\tau = 0.8$ s, as per (2). This scenario is evaluated with and without disturbances. When disturbances are considered, each follower node is subjected to a constant disturbance, and the disturbance vector is $w = [0.15\ 0.25\ 0.08\ 0.4]^\top$. The Predecessor-Follower with Leader (PFL) topology is employed for the FOPID controller, while the Two-Predecessor-Follower with Leader (TPFL) and Bidirectional with Leader (BDL) topologies are adopted for the FOPD and TID controllers, respectively. Moreover, for sketching the stability region in a 2D space, some control parameters are fixed as follows. For the FOPID, $\mu = 0.8$ and $K_D = 5$; for the FOPD solution, $\mu = 1.2$; and for the TID strategy, the $n$-parameter is $n = 3$ and $K_D = 5$. The stability regions, computed via the corresponding theorems for each control solution, are illustrated in Figure 3.

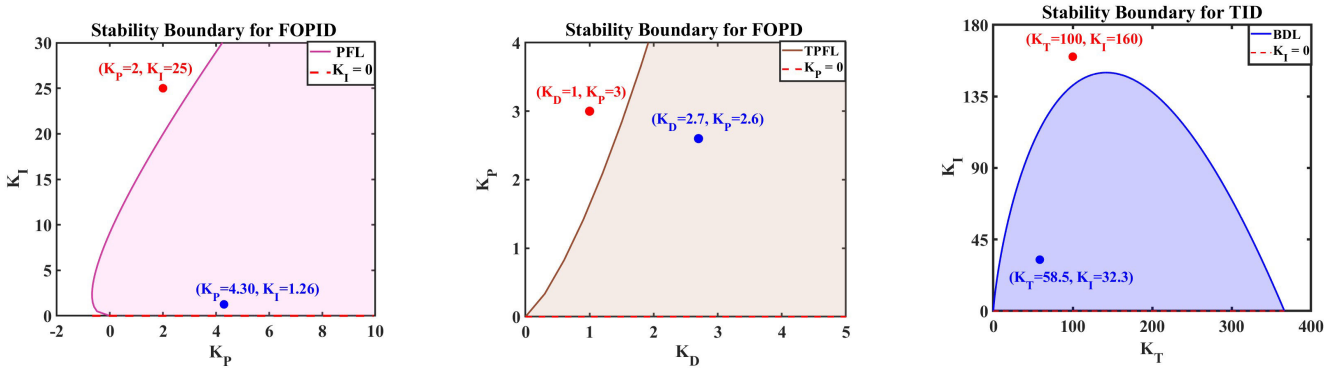


**FIGURE 3.** Stability boundaries for each novel FOC: (a) FOPID; (b) FOPD; and (c) TID.

The remaining control parameters are tuned using a Genetic Algorithm (GA) approach. Specifically, the GA strategy targets the minimisation of the Integral Absolute Error (IAE) cost function, defined as:

$$\begin{aligned}\text{IAE} = \sum_{i=1}^{N} \Bigg[ & q_1 \int_0^t \left| s_0(t) - s_i(t) - d_{0,i} \right| dt \\ & + q_2 \int_0^t \left| v_0(t) - v_i(t) \right| dt \\ & + q_3 \int_0^t \left| a_0(t) - a_i(t) \right| dt \Bigg], \end{aligned} \tag{122}$$

where $q_1$, $q_2$, $q_3$ are positive constant weights. Figure 4 depicts the cost function IAE within the stable region as a contour plot, highlighting the GA-identified minimum for each controller.

The simulation results demonstrate the theoretical findings. For the FOPID controller, Figure 5a shows that the intravehicular distance error between each follower and the leader diverges when the parameters $(K_P, K_I)$ are selected from the unstable region indicated in Figure 3. Conversely, when a stable parameterisation is used, the tracking error converges to zero, also in the presence of constant disturbances acting on each node, as depicted in Figure 5b. This outcome is in agreement with Theorem 1. Similar validation results are obtained for the FOPD and TID algorithms. Specifically, Figs. 6a and 7a illustrate an unbounded drift of the relative distance errors when the control parameters are within the unstable regions. When control parameters are selected from within the stable regions, Figs. 6b and 7b confirm the stability of the closed-loop system and demonstrate the presence of a steady-state error under constant disturbances. These observed errors align closely with those predicted theoretically via (96) for FOPD and (119) for TID, as quantitatively summarised in Table 1. Finally, in the absence of disturbances, the position tracking error converges to zero, as depicted in Figs. 6c and 7c. This behaviour is consistent with Theorem 2 and Theorem 3, respectively.

**TABLE 1.** Comparison of theoretical and simulated steady-state spacing errors under constant disturbances.

| Error Source | Distributed FOPD | | Distributed TID | |
|---|---|---|---|---|
| | Theorem 2 | Simulation | Theorem 3 | Simulation |
| Leader–Follower 1 | -0.0568 | -0.0568 | -0.0043 | -0.0041 |
| Leader–Follower 2 | -0.0473 | -0.0474 | -0.0039 | -0.0037 |
| Leader–Follower 3 | -0.0599 | -0.0600 | -0.0043 | -0.0042 |
| Leader–Follower 4 | -0.0420 | -0.0421 | -0.0029 | -0.0028 |

### B. WLTP-BASED PERFORMANCE EVALUATION

In this scenario, the performance of the fractional-order controllers is evaluated when the leader's speed profile is the Worldwide harmonised Light vehicles Test Procedure (WLTP) cycle, incorporating also external disturbances. The evaluation considers three platoon lengths with six different topologies, namely, PF, PFL, BD, BDL, TPF, and TPFL. The initial inter-vehicle spacing between the leader and each follower is set at the desired spacing of 20 m. The follower vehicles, along with the leader, start from rest. The WLTP manoeuvre consists of four distinct phases as illustrated in Figure 8 where:

- **Phase 1 ($P_1$).** The leader follows the low-speed WLTP segment from 0 to 600 s, characterised by frequent stops and accelerations. The velocity varies from standstill to approximately 15.6 m/s.
- **Phase 2 ($P_2$).** The leader executes the medium-speed WLTP segment from 600 to 1015 s with velocities reaching around 21 m/s.
- **Phase 3 ($P_3$).** The leader performs the high-speed WLTP segment 1015 to 1475 s where the maximum speed is around 27 m/s. External disturbances continue to affect the followers during this phase.
- **Phase 4 ($P_4$):** The leader follows the extra-high speed WLTP segment from 1475 to 1800 s, reaching approximately 36 m/s.

The external disturbances are applied during Phases 2 and 3 and vary according to the platoon size $N$ as follows: The external disturbances are applied during Phases

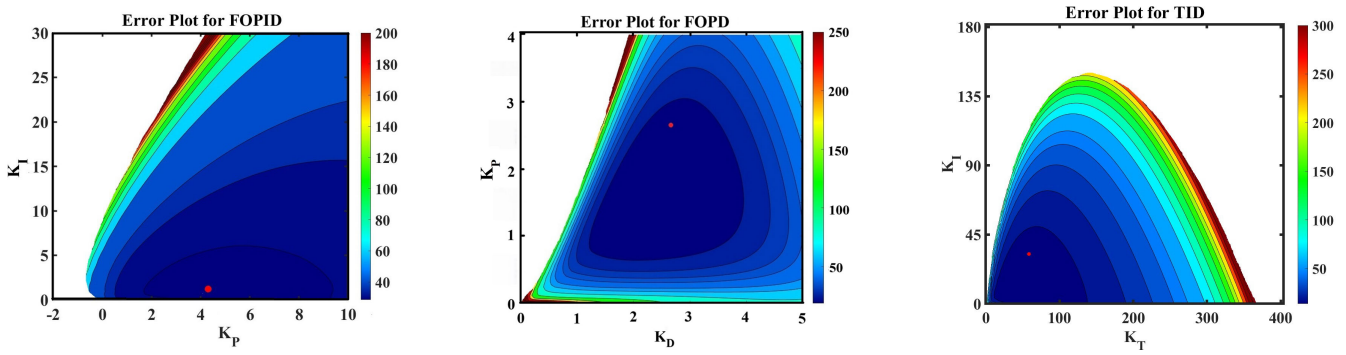


**FIGURE 4.** Contour error plots showing the variation of the IAE within the stable region for the three novel fractional-order controllers: (a) FOPID, (b) FOPD, (c) TID.

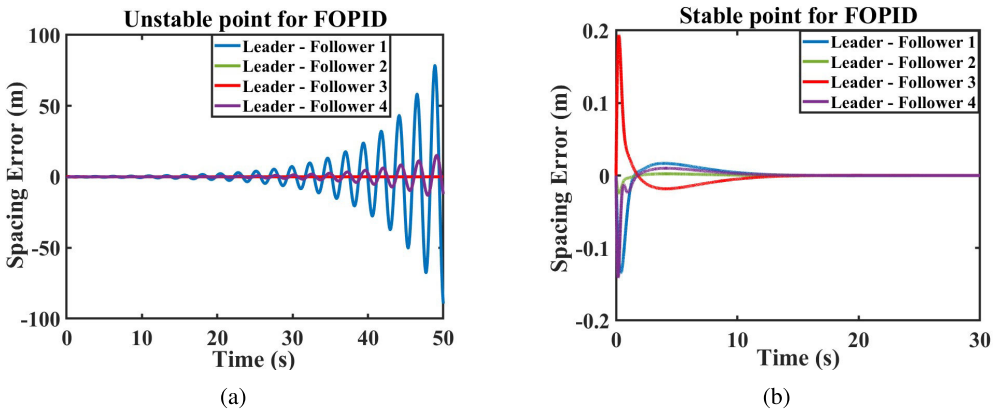


**FIGURE 5.** Spacing error for FOPID: (a) At an unstable point. (b) At a stable point with external disturbances.

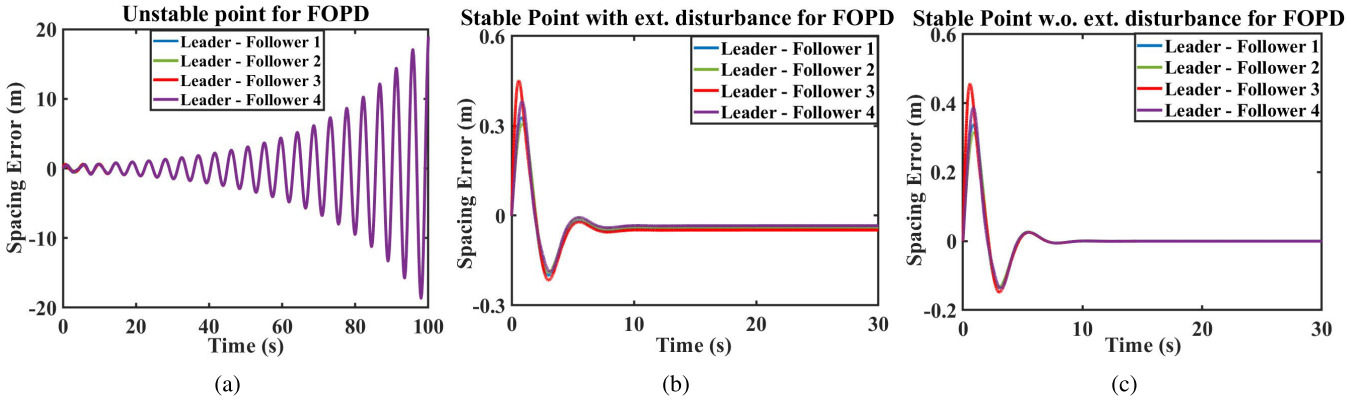


**FIGURE 6.** Spacing error for FOPD: (a) At an unstable point. (b) At a stable point with external disturbances. (c) At a stable point without external disturbances.

2 and 3 and vary according to the platoon size $N$ as follows:

$$\begin{aligned} N = 4 &\Rightarrow \bar{w} = [0.04, 0.08, -0.05, -0.03], \\ N = 8 &\Rightarrow \bar{w} = [0.04, 0.08, -0.05, -0.03, \\ &\quad 0.12, -0.09, 0.03, -0.15], \\ N = 12 &\Rightarrow \bar{w} = [0.04, 0.08, -0.05, -0.03, 0.12, -0.09, \\ &\quad 0.03, -0.15, 0.06, 0.10, -0.07, 0.06]. \end{aligned} \tag{123}$$

The closed-loop dynamics provided by the fractional-order control strategies have been compared against the corresponding integer-order control formulation by using a set of key performance indicators (KPIs). Specifically, by defining the tracking errors for each phase $P_j, j = 1, \ldots, 4$ as

$$E_{\sigma,P_j} = \max_{i\in\{1,2,\ldots,N\}} \left( \max_{t\in P_j} |\sigma_i(t)| \right), \tag{124}$$

where $\sigma \in \{\tilde{s}, \tilde{v}, \tilde{a}\}$ represents position, velocity, or acceleration error, respectively. The closed-loop tracking

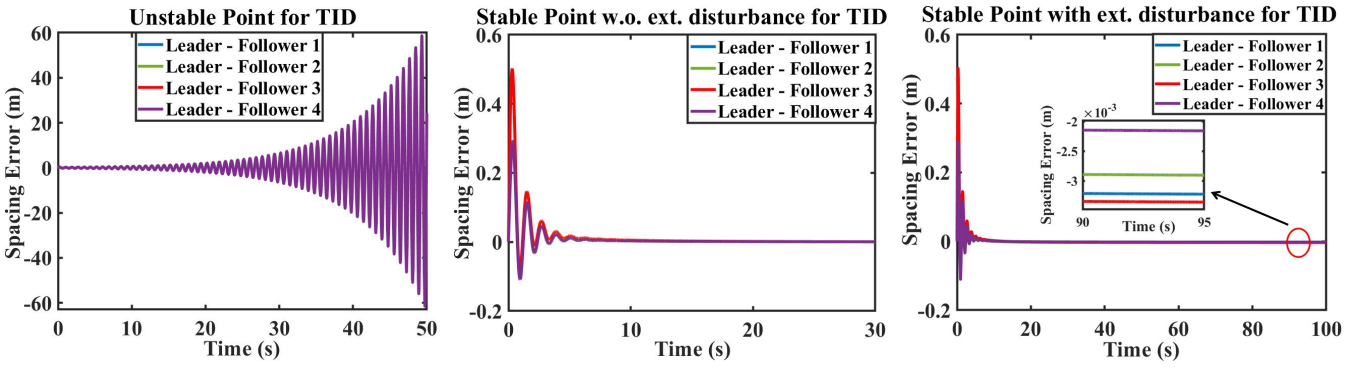


**FIGURE 7.** Spacing error for TID: (a) At an unstable point. (b) At a stable point with external disturbances. (c) At a stable point without external disturbances.

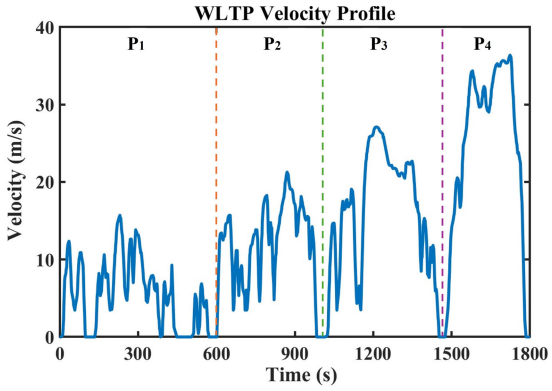


**FIGURE 8.** WLTP profile with four phases: $P_1$, $P_2$, $P_3$, and $P_4$.

**TABLE 2.** Simulation results — PID vs FOPID controllers.

| N. | Top. | Peak Spacing (m) | | | | Peak Velocity (m/s) | | | |
|---|---|---|---|---|---|---|---|---|---|
| | | $P_1$ | $P_2$ | $P_3$ | $P_4$ | $P_1$ | $P_2$ | $P_3$ | $P_4$ |
| 4 | PF | 16.12 | 13.3 | 12.01 | 10.65 | 4.19 | 15.61 | 5.43 | 10.66 |
| 4 | PFL | 15.98 | 14.88 | 12.98 | 11.41 | 11.58 | 10.44 | 16.96 | 19.88 |
| 4 | BD | 19.13 | 13.36 | 12.61 | 20.33 | 17.95 | 15.86 | 6.07 | 26.8 |
| 4 | BDL | 15.97 | 14.82 | 12.99 | 11.65 | 11.45 | 10.2 | 16.94 | 18.8 |
| 4 | TPF | 16.3 | 18.56 | 13.6 | 12.96 | 11.62 | 10.13 | 17.42 | 21.69 |
| 4 | TPFL | 16.06 | 14.85 | 13.02 | 11.41 | 11.46 | 10.47 | 16.97 | 18.73 |
| 8 | PF | 46.12 | 41.98 | 38.7 | 48.25 | 44.46 | 39.81 | 36.29 | 40.79 |
| 8 | PFL | 15.98 | 14.81 | 12.99 | 11.44 | 11.58 | 10.31 | 16.98 | 19.64 |
| 8 | BD | 22.82 | 12.7 | 29.38 | 17.21 | 29.69 | 24.26 | 19.66 | -10.59 |
| 8 | BDL | 15.97 | 14.35 | 12.99 | 11.51 | 11.4 | 10.57 | 16.99 | 18.99 |
| 8 | TPF | 32.95 | 33.18 | 28.04 | 15.57 | 45.71 | 40.63 | 42.65 | 39.14 |
| 8 | TPFL | 15.94 | 15.91 | 12.98 | 11.44 | 11.33 | 33.45 | 16.98 | 54.48 |
| 12 | PF | 58.29 | 55.7 | 49.55 | 57.95 | 56.48 | 53.11 | 47.58 | 52.77 |
| 12 | PFL | 16.05 | 71.38 | 12.98 | 65.58 | 11.23 | 90.87 | 17 | 93.03 |
| 12 | BD | 16.49 | 54.83 | -23.95 | 31.48 | 26.47 | 56.87 | -10.91 | 35.65 |
| 12 | BDL | 15.97 | 14.85 | 13 | 11.53 | 11.43 | 10.23 | 16.97 | 19 |
| 12 | TPF | 74.43 | 74.55 | 75.6 | 80.27 | 77.04 | 74.89 | 77.4 | 80.05 |
| 12 | TPFL | 16.04 | 90.52 | 12.98 | 89.24 | 11.43 | 97.8 | 16.97 | 97.83 |

performance improvement given by the fractional order solution over its integer order counterpart is measures via the following KPIs:

$$\Delta_{\sigma,P_j} = \frac{E_{\sigma,P_j,\text{integer}} - E_{\sigma,P_j,\text{fractional}}}{E_{\sigma,P_j,\text{integer}}} \times 100, \qquad (125)$$

where "fractional" and "integer" refer to a fractional order controller proposed in Section IV and its corresponding integer order counterpart, respectively.

**TABLE 3.** Simulation results — PD vs FOPD controllers.

| N. | Top. | Peak Spacing (m) | | | | Peak Velocity (m/s) | | | | Peak Accel. (m/s²) | | | |
|---|---|---|---|---|---|---|---|---|---|---|---|---|---|
| | | $P_1$ | $P_2$ | $P_3$ | $P_4$ | $P_1$ | $P_2$ | $P_3$ | $P_4$ | $P_1$ | $P_2$ | $P_3$ | $P_4$ |
| 4 | PF | 42.86 | 36.23 | 32.75 | 46.37 | 61.89 | 54.66 | 45.33 | 56.53 | 50.93 | 64.07 | 60.46 | 64.74 |
| 4 | PFL | 33.08 | 35.57 | 31.56 | 36.67 | 37.4 | 44.65 | 41.96 | 26.03 | 51.39 | 55.65 | 45.04 | 20.76 |
| 4 | BD | 31.02 | 29.67 | 29.72 | 37.15 | 22.99 | 26.07 | 26.98 | 28.2 | 20.54 | 16.62 | 10.49 | 19.98 |
| 4 | BDL | 33.08 | 35.51 | 31.29 | 36.67 | 37.4 | 44.65 | 41.97 | 26.02 | 51.31 | 55.66 | 45.02 | 20.71 |
| 4 | TPF | 37.07 | 36.4 | 31.92 | 36.9 | 45.8 | 51.69 | 50.11 | 27.13 | 66.31 | 55.15 | 47.99 | 15.89 |
| 4 | TPFL | 33.08 | 35.57 | 31.56 | 36.67 | 37.4 | 44.66 | 41.98 | 26.03 | 51.37 | 55.67 | 45.06 | 20.67 |
| 8 | PF | 71.19 | 78.06 | 72.65 | 66.63 | 82.6 | 89.61 | 86.32 | 87.03 | 83.39 | 93.67 | 91.8 | 87.68 |
| 8 | PFL | 33.08 | 35.57 | 30.4 | 36.67 | 37.4 | 44.65 | 41.96 | 26.03 | 51.39 | 55.66 | 45.04 | 21.66 |
| 8 | BD | 42.97 | 31.18 | 11.53 | 26.28 | 27.83 | 23.5 | 1.8 | 5.88 | -4.05 | -16.96 | -17.67 | 6.81 |
| 8 | BDL | 33.08 | 34.34 | 29.61 | 36.67 | 37.39 | 44.65 | 41.97 | 26.03 | 51.4 | 55.63 | 45.03 | 20.67 |
| 8 | TPF | 47.23 | 51.02 | 39.06 | 42.23 | 80.98 | 66.76 | 68.16 | 77.02 | 81.88 | 81.16 | 75.89 | 81.53 |
| 8 | TPFL | 33.08 | 35.57 | 31.36 | 36.67 | 37.4 | 44.65 | 41.95 | 26.05 | 51.39 | 55.66 | 45.04 | 20.67 |
| 12 | PF | 94.22 | 96.37 | 95.21 | 91.4 | 96.23 | 98.6 | 98.28 | 96.83 | 97 | 98.72 | 98.49 | 96.5 |
| 12 | PFL | 33.09 | 35.57 | 30.4 | 36.67 | 37.4 | 44.65 | 41.96 | 26.04 | 51.37 | 55.66 | 45.04 | 38.07 |
| 12 | BD | 20.81 | 2.88 | 52.65 | 27.18 | 17.03 | -26.98 | 25 | 4.61 | 15.68 | -36.65 | 6.41 | 12.06 |
| 12 | BDL | 33.08 | 35.52 | 30.35 | 36.67 | 37.4 | 44.65 | 41.97 | 26.02 | 51.38 | 55.64 | 45.03 | 20.68 |
| 12 | TPF | 91.5 | 84.96 | 75.46 | 79.73 | 97.7 | 93.28 | 92.64 | 94.75 | 97.76 | 96.15 | 93.5 | 95.6 |
| 12 | TPFL | 33.08 | 35.57 | 31.36 | 36.67 | 37.39 | 44.66 | 41.97 | 38.95 | 51.4 | 55.66 | 45.04 | 68.88 |

**TABLE 4.** Simulation results — PID vs TID controllers.

| N. | Top. | Peak Spacing (m) | | | | Peak Velocity (m/s) | | | | Peak Accel. (m/s²) | | | |
|---|---|---|---|---|---|---|---|---|---|---|---|---|---|
| | | $P_1$ | $P_2$ | $P_3$ | $P_4$ | $P_1$ | $P_2$ | $P_3$ | $P_4$ | $P_1$ | $P_2$ | $P_3$ | $P_4$ |
| 4 | PF | 21.44 | 20.03 | 21.2 | 19.67 | 21.48 | 19.44 | 19.93 | 20.68 | 17.91 | 17.66 | 19.43 | 20.49 |
| 4 | PFL | 20.59 | 19.56 | 20.49 | 19.3 | 20.7 | 17.89 | 18.42 | 19.4 | 21.54 | 14.79 | 17.01 | 18.65 |
| 4 | BD | 25.16 | 28.88 | 28.57 | 18.09 | 18.02 | 16.77 | 21.38 | 9.22 | 14.73 | 4.07 | 17.02 | 6.96 |
| 4 | BDL | 20.59 | 19.57 | 20.49 | 19.3 | 20.7 | 17.92 | 18.45 | 19.45 | 21.78 | 14.74 | 17.02 | 18.4 |
| 4 | TPF | 20.78 | 19.66 | 20.56 | 19.36 | 20.94 | 18.27 | 18.83 | 19.79 | 21.25 | 15.51 | 17.58 | 19.43 |
| 4 | TPFL | 20.59 | 19.56 | 20.75 | 19.3 | 20.7 | 17.93 | 18.46 | 19.45 | 21.14 | 14.75 | 15.74 | 18.37 |
| 8 | PF | 22.35 | 22.7 | 22.27 | 20.38 | 19.69 | 21.01 | 21.42 | 19.8 | 21.28 | 19.88 | 19.74 | 20.57 |
| 8 | PFL | 20.59 | 19.56 | 20.43 | 19.29 | 20.68 | 17.9 | 18.45 | 19.41 | 21.81 | 14.78 | 17.02 | 18 |
| 8 | BD | 11.41 | 24.18 | 21.84 | 16.42 | 0.54 | 13.42 | 15.17 | 7.27 | -17.58 | 16.98 | 0.19 | -13.47 |
| 8 | BDL | 20.59 | 19.57 | 20.43 | 19.3 | 20.7 | 17.93 | 18.45 | 19.36 | 21.46 | 14.23 | 16.59 | 17.5 |
| 8 | TPF | 21.15 | 19.86 | 20.84 | 19.5 | 21.36 | 18.98 | 19.55 | 20.42 | 16.94 | 16.87 | 19 | 20.64 |
| 8 | TPFL | 20.59 | 19.56 | 20.51 | 19.3 | 20.69 | 17.93 | 18.46 | 19.45 | 21.45 | 14.23 | 16.37 | 18.63 |
| 12 | PF | 25.25 | 24.27 | 23.23 | 21.37 | 23.08 | 21.73 | 22.64 | 21.95 | 24.07 | 21.2 | 23.78 | 20.26 |
| 12 | PFL | 20.59 | 19.56 | 20.44 | 19.3 | 20.66 | 17.91 | 18.46 | 19.43 | 21.35 | 14.74 | 16.78 | 18.29 |
| 12 | BD | 25.6 | 32.3 | 12.42 | 19.69 | 27.45 | 36.24 | 0.41 | 3.95 | 17.56 | 23.46 | -21.9 | -2.41 |
| 12 | BDL | 20.59 | 19.57 | 20.46 | 19.3 | 20.7 | 17.92 | 18.46 | 19.4 | 20.88 | 14.23 | 16.92 | 17.89 |
| 12 | TPF | 21.53 | 20.05 | 21.24 | 19.68 | 21.69 | 19.68 | 20.23 | 20.98 | 18.46 | 18.14 | 19.81 | 21.34 |
| 12 | TPFL | 20.59 | 19.56 | 20.46 | 19.3 | 20.69 | 17.93 | 18.46 | 19.42 | 21.58 | 14.79 | 16.89 | 18.45 |

**TABLE 5.** Nominal parameters for heterogeneous platoon nodes.

| Vehicle Index ($i$) | $R_{wi}$ (m) | $M_i$ (kg) | $\eta_i$ (-) | $C_{A,i}$ (kg/m) | $\tau_i$ (s) | $f_{ri}$ (-) |
|---|---|---|---|---|---|---|
| 1 | 0.285 | 1445 | 0.80 | 0.41 | 0.8 | 0.022 |
| 2 | 0.290 | 1550 | 0.82 | 0.42 | 0.9 | 0.019 |
| 3 | 0.275 | 1450 | 0.87 | 0.44 | 0.6 | 0.021 |
| 4 | 0.281 | 1400 | 0.83 | 0.47 | 0.5 | 0.023 |
| 5 | 0.278 | 1600 | 0.81 | 0.46 | 0.4 | 0.024 |

The gains of the proposed control solutions have been tuned by considering a two-stage approach. Specifically, in the first stage, the stability conditions on the control gains are derived for each fractional order controller (FOPID, FOPD, TID) using either Theorem 1, 2 or 3. Subsequently, in the second stage, to find the optimal control parameters,

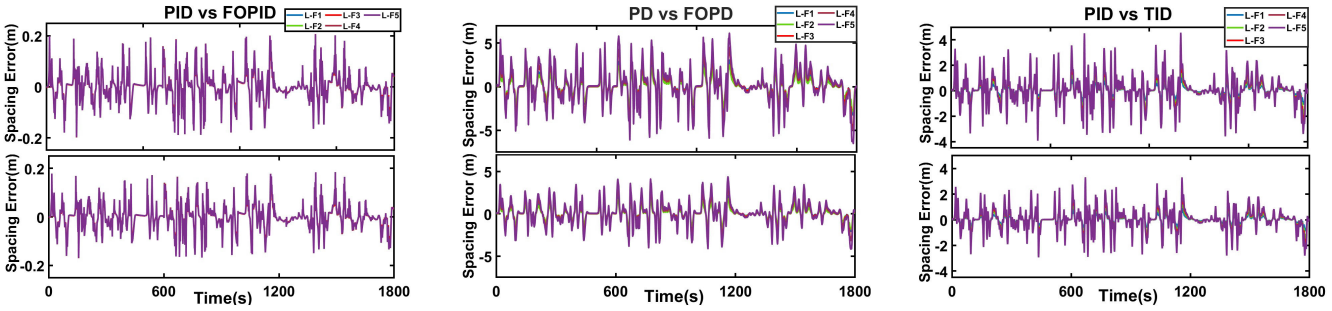


**FIGURE 9.** Robust analysis: (a) PID (above) and FOPID (below) in the case of PFL topology;(b) PD (above) and FOPD (below) in the case of TPF topology;(c) PID (above) and TID (below) in the case of BD topology.

**TABLE 6.** Robust analysis.

| N | Top. | Peak Spacing [%] | | | | Peak Velocity [%] | | | | Peak Acceleration [%] | | | |
|---|---|---|---|---|---|---|---|---|---|---|---|---|---|
| | | P1 | P2 | P3 | P4 | P1 | P2 | P3 | P4 | P1 | P2 | P3 | P4 |
| | PID vs FOPID | | | | | | | | | | | | |
| 5 | PF | 13.81 | 12.52 | 9.77 | 11.36 | -2.3 | -5.19 | 2.52 | 11.3 | - | - | - | - |
| 5 | PFL | 13.37 | 11.38 | 11.38 | 8.95 | 8.8 | 8.99 | 10.85 | 9.61 | - | - | - | - |
| 5 | BD | 15.92 | 10.34 | 17.92 | 5.06 | -5.68 | 10.37 | 1.99 | 1.06 | - | - | - | - |
| 5 | BDL | 13.07 | 11.4 | 11.36 | 8.96 | 8.38 | 8.47 | 10.27 | 9.52 | - | - | - | - |
| 5 | TPF | 12.29 | 13.33 | 11.67 | 9.94 | 9.04 | 7.24 | 10.61 | 10.93 | - | - | - | - |
| 5 | TPFL | 12.71 | 11.21 | 11.32 | 9.03 | 8.51 | 8.86 | 10.39 | 9.73 | - | - | - | - |
| | PD vs FOPD | | | | | | | | | | | | |
| 5 | PF | 40.29 | 34.35 | 34.25 | 43.48 | 56.14 | 50.22 | 45.36 | 47.05 | 55.21 | 59.35 | 52.3 | 40.77 |
| 5 | PFL | 29.44 | 32.79 | 28.59 | 36.38 | 36.73 | 41.1 | 38.76 | 22.85 | 9.57 | 5.65 | 7.27 | -2.5 |
| 5 | BD | 23.69 | 22.2 | 32.58 | 39.88 | 8.92 | 18.69 | 19.42 | 19.68 | -3.05 | -3.04 | 10.75 | -5.35 |
| 5 | BDL | 29.67 | 33.68 | 28.58 | 36.4 | 37.34 | 45.13 | 42.03 | 25.69 | 18.79 | 8.71 | 7.21 | -3.81 |
| 5 | TPF | 32.12 | 32.8 | 28.84 | 36.04 | 39.25 | 44.41 | 43.46 | 25.11 | 38.84 | 36.66 | 21.63 | 4.53 |
| 5 | TPFL | 29.43 | 32.79 | 28.59 | 36.38 | 36.73 | 41.1 | 38.76 | 22.84 | 9.42 | 7.22 | 8.09 | -8.98 |
| | PID vs TID | | | | | | | | | | | | |
| 5 | PF | 21.44 | 20.05 | 21.48 | 19.78 | 21.41 | 19.2 | 19.7 | 20.3 | 3.83 | 2.15 | 2.85 | 2.03 |
| 5 | PFL | 20.64 | 19.65 | 20.64 | 19.4 | 20.73 | 18.02 | 18.52 | 19.46 | 0.67 | 0.28 | 0.58 | 0.29 |
| 5 | BD | 25.38 | 26.52 | 27.53 | 17.61 | 23.49 | 16.87 | 23.29 | 9.56 | 7.3 | -2.94 | 7.99 | 2.1 |
| 5 | BDL | 20.59 | 19.61 | 20.61 | 19.35 | 20.7 | 17.91 | 18.44 | 19.41 | 0.64 | 0.27 | 0.57 | 0.28 |
| 5 | TPF | 20.82 | 19.74 | 20.94 | 19.51 | 20.89 | 18.26 | 18.73 | 19.57 | 1.77 | 0.8 | 1.4 | 1.07 |
| 5 | TPFL | 20.64 | 19.65 | 20.64 | 19.4 | 20.73 | 18.02 | 18.52 | 19.46 | 0.78 | 0.34 | 0.63 | 0.37 |

a GA method is used to optimise the cost function (122) over the WLTP manoeuvre. The search space for the GA algorithm is constrained by the stability boundaries derived in the first stage. This systematic methodology guarantees closed-loop stability while simultaneously achieving optimal controller parameters. For a fair comparison, the same approach has also been used for the tuning of the integer-order controllers, where the stability regions for PID and the PD solutions are obtained leveraging the results presented in [73] and [74], respectively.

Tables 2–4 summarise the results for each phase.

Based on these tables the following the following remarks can be drawn.

- **FOPID vs. PID (Table 2).** The FOPID controller outperforms the PID strategy also in the presence of external disturbances. For instance a substantial reductions in peak spacing and velocity error can be observed, especially in larger platoons (e.g., for N = 12, in the case of the TPFL topology during the P2 phase, this reduction in spacing error and speed is up to 90.52% and 97.8%, respectively), thus also confirming that fractional order strategies can better suppress disturbances.
- **FOPD vs. PD (Table 3).** The FOPD controller provides better closed-loop tracking performance compared to its integer counterpart, with significant KPI improvements in spacing, velocity, and acceleration (e.g., when N=12, and in the case of the PF topology, there is a reduction up to 96.37% and 98.72% for spacing and acceleration peak errors over the P2-phase).
- **TID vs. PID (Table 4).** The TID controller demonstrates a consistent improvement over PID, with spacing and velocity error KPIs often in the 20-30% range (e.g., N=12, BD topology P2 spacing KPI of 32.3% and velocity KPI of 36.24%).

### C. ROBUSTNESS ANALYSIS

This section evaluates the robustness of the proposed fractional-order control strategies and compares their performance with that of the integer-order controller counterparts. Specifically, the simulation scenario considers a heterogeneous platoon with five follower vehicles. Each vehicle is modelled through the nonlinear modelling approach presented in [60] and [75]. Hence, each vehicle is characterised with a different set of parameters consisting of the vehicle mass ($M_i$), aerodynamic drag coefficient ($C_{A,i}$), tyre radius

($R_{wi}$), powertrain time constant ($\tau_i$), driveline efficiency ($\eta_i$), and rolling resistance ($f_{ri}$). The values for the vehicle's parameters are given in Table 5. Moreover, each vehicle is equipped with the low-level static feedback linearisation control strategy presented in [58] However, for the tuning of this low-level controller, it is assumed that only nominal vehicle parameters are known, which differ from the actual ones by up to $\pm 10$ %. Hence, the vehicle nonlinearities are not perfectly compensated, and thus each follower is subjected to state-dependent nonlinear disturbance. The leader's speed profile is the WLTP cycle in Figure 8.

Figure 9 depicts the residual tracking error and shows that proposed the fractional-order strategies outperform the corresponding integer-order counterparts.

The closed-loop tracking performance are quantitatively evaluated also through the use of the KPIs introduced in Section VIII, and results are collected in Table 6 for each phase of the WLTP manoeuvrer and for different topologies. Table 6 shows that, beside few operating conditions, the novel fractional-order control methods provide smaller tracking errors compared to the integer-order solutions, thus improving robustness to residual unmodelled nonlinear dynamics.

## IX. CONCLUSION

This paper presented three novel distributed fractional-order controllers—FOPID, FOPD, and TID—for vehicle platoons with second- and third-order longitudinal dynamics. Stability conditions were systematically derived using the Root Boundary Locus approach. Extensive simulation analysis confirmed that these novel fractional-order controllers can outperformance their integer-order counterparts by providing reduced closed-loop tracking error dynamics. For instance, under WLTP tests with external disturbances, FOPID and FOPD significantly reduced the peak spacing error up to 90.52% and 96.37%, respectively, for a vehicle platoon with twelve followers. Similarly, the TID controller showed consistent improvements in reducing tracking errors across all considered platoon lengths and the six topologies. Moreover, the FOCs demonstrated improved robustness to external disturbances and parameter uncertainties in heterogeneous platoons, plus scalability across varying platoon sizes. Hence, future work will target the extension of the proposed FOC strategies and the analytical study of the closed-loop dynamics to heterogeneous platoon, communication time delays and parameteric uncertainties.

## APPENDIX A
## FRACTIONAL CALCULUS

Fractional order controller algorithms utilise fractional calculus for the design of the control action. Fractional calculus generalises integer-order differentiation and integration to non-integer orders. However, the extension of the concept of integrals and derivatives with fractional order is not unique and several definitions can be found in the literature [76]. In this paper, Caputo's fractional order integral and derivative definitions are adopted and reported below.

*Definition 1 (Caputo Fractional Integral [70], [76]):* Consider the function $f$ defined in $(t_0, +\infty)$, its integral of order $\lambda > 0$ for any time instant $t > t_0$ is given as:

$$ {}_{t_0}D_t^{-\lambda} f(t) = \frac{1}{\Gamma(\lambda)} \int_{t_0}^{t} (t-\zeta)^{\lambda-1} f(\zeta)\, d\zeta. \tag{126} $$

*Definition 2 (Caputo Fractional Derivative [70], [76]):* Consider a smooth function $f$ defined in $(t_0, +\infty)$, its derivative of order $\mu > 0$ for any time instant $t > t_0$ is given as:

$$ {}_{t_0}D_t^{\mu} f(t) = \frac{1}{\Gamma(n-\mu)} \int_{t_0}^{t} \frac{f^{(n)}(\zeta)}{(t-\zeta)^{\mu+1-n}}\, d\zeta, \tag{127} $$

where $n$ is the smallest integer greater than $\mu$. In Definitions 126 and 127, $\Gamma$ is the Euler's Gamma function. By denoting with $F$ the Laplace transform of $f$, it is possible to prove that [70], [76]:

$$ L\{{}_{t_0}D_t^{-\lambda} f(t)\} = s^{-\lambda} F(s), \tag{128} $$

and

$$ L\{{}_{t_0}D_t^{\mu} f(t)\} = s^{\mu} F(s) - \sum_{k=0}^{n-1} s^{\mu-k-1}\, {}_{t_0}D^k f(t)\big|_{t=0}, \tag{129} $$

where $L$ is the Laplace operator.

## APPENDIX B
## ROOT BOUNDARY LOCUS APPROACH

Consider the characteristic equation of a SISO linear system in the Laplace domain as:

$$ F(\alpha, \beta, s) = 0, \tag{130} $$

where $\alpha$ and $\beta$ are two system parameters that appear linearly in (130). The Root Boundary Locus (RBL) approach is employed to find the regions of the $(\alpha, \beta)$-plane (i.e., the conditions on the parameters $\alpha$ and $\beta$) for which the system is asymptotically stable. To achieve this, conditions on the system parameters for which the characteristic polynomial (130) has poles crossing the imaginary axis are first derived. These conditions divide the $(\alpha, \beta)$-plane into regions, and the implicit function theorem is then used to identify zones in the parameter space that guarantee asymptotic stability. Specifically, the characteristic polynomial (130) has roots on the imaginary axis at position $j\omega$ when:

$$ F_1(\alpha, \beta, \omega) = F_2(\alpha, \beta, \omega) = 0, \tag{131} $$

where $F_1(\alpha, \beta, \omega) = \mathrm{Re}\, F(\alpha, \beta, j\omega)$ and $F_2(\alpha, \beta, \omega) = \mathrm{Im}\, F(\alpha, \beta, j\omega)$, respectively. Solutions of (131) for $\omega \in (0, +\infty)$ define boundaries that divide the parameter plane into stable and unstable regions. According to [77], the study of the Jacobian:

$$ \tilde{J} = \begin{bmatrix} \dfrac{\partial F_1}{\partial \alpha} & \dfrac{\partial F_1}{\partial \beta} \\ \dfrac{\partial F_2}{\partial \alpha} & \dfrac{\partial F_2}{\partial \beta} \end{bmatrix}, \tag{132} $$

not only determines when solutions of (131) are locally represented by curves parameterised by increasing $\omega$, but

also helps establish which side of the curve corresponds to the stable region. Indeed, if the point $(\alpha_0, \beta_0)$ is a solution of (131) for a given $\omega_0$, and the Jacobian (132) is non-singular at $(\alpha_0, \beta_0, \omega_0)$, then according to the implicit function theorem, there exists a neighbourhood of $\omega_0$ for which the solutions of (131) are given by a curve $(\alpha(\omega), \beta(\omega))$. The functions $\alpha(\omega)$ and $\beta(\omega)$ satisfy $F_1(\alpha(\omega), \beta(\omega), \omega) = F_2(\alpha(\omega), \beta(\omega), \omega) = 0$. Moreover, as discussed in [77], the determinant of the Jacobian in (132) can be used to identify the stability region in the $(\alpha, \beta)$-plane.

*Proposition 1:* The critical roots are in the right half-plane if the point in the parameter plane, relative to selected values of $\alpha$ and $\beta$, lies on the left side of the curve $(\alpha(\omega), \beta(\omega))$ when following this curve in the direction of increasing $\omega$, whenever $\det(\tilde{J}) < 0$, and on the right side when $\det(\tilde{J}) > 0$. From a practical viewpoint, Proposition 1 states that when following the $(\alpha(\omega), \beta(\omega))$-curve in the direction of increasing $\omega$, the region of the $(\alpha, \beta)$-plane guaranteeing asymptotic stability of the system is on the right of the curve when $\det(\tilde{J}(\alpha(\omega), \beta(\omega), \omega)) < 0$, otherwise it is on the left of the curve when $\det(\tilde{J}(\alpha(\omega), \beta(\omega), \omega)) > 0$. Singular values of the Jacobian $\tilde{J}$ do not allow determining the local curve in the parameter space and the study of the stable region. Finally, according to [77], the boundary curves between the stable and unstable regions in the $(\alpha, \beta)$-plane are the union of the following three boundaries:

- Real root boundary (RRB) obtained from (131) when $\omega = 0$ (i.e., the imaginary axis is crossed by a real pole).
- Complex root boundary (CRB) obtained from (131) when $\omega \in (0, \infty)$ (i.e., the imaginary axis is crossed by a pair of complex poles).
- Infinite root boundary (IRB) obtained from (131) when $\omega \to +\infty$.

The reader is referred to [77] and [78] for further details about the RBL approach for conditional stability.

## ACKNOWLEDGMENT

The authors would like to express their sincere gratitude to Kehkashan Qaiser for her contribution to the simulation part.

## REFERENCES

[1] U. Montanaro, S. Dixit, S. Fallah, M. Dianati, A. Stevens, D. Oxtoby, and A. Mouzakitis, "Towards connected autonomous driving: Review of use-cases," *Vehicle Syst. Dyn.*, vol. 57, no. 6, pp. 779–814, Jun. 2019.

[2] A. Alam, B. Besselink, V. Turri, J. Mårtensson, and K. H. Johansson, "Heavy-duty vehicle platooning for sustainable freight transportation: A cooperative method to enhance safety and efficiency," *IEEE Control Syst. Mag.*, vol. 35, no. 6, pp. 34–56, Dec. 2015.

[3] S. E. Li, Y. Zheng, K. Li, Y. Wu, J. K. Hedrick, F. Gao, and H. Zhang, "Dynamical modeling and distributed control of connected and automated vehicles: Challenges and opportunities," *IEEE Intell. Transp. Syst. Mag.*, vol. 9, no. 3, pp. 46–58, Fall. 2017.

[4] Y. Li, Z. Qin, H. Zhu, S. Peeta, and X. Gao, "Platoon control of connected vehicles with heterogeneous model structures considering external disturbances," *Green Energy Intell. Transp.*, vol. 1, no. 3, Dec. 2022, Art. no. 100038.

[5] Y. Zheng, S. Eben Li, J. Wang, D. Cao, and K. Li, "Stability and scalability of homogeneous vehicular platoon: Study on the influence of information flow topologies," *IEEE Trans. Intell. Transp. Syst.*, vol. 17, no. 1, pp. 14–26, Jan. 2016.

[6] Y. Zhou, S. Ahn, M. Wang, and S. Hoogendoorn, "Stabilising mixed vehicular platoons with connected automated vehicles: An $H_\infty$ approach," *Transp. Res. B, Methodol.*, vol. 132, pp. 152–170, Feb. 2020.

[7] C. Quadri, V. Mancuso, M. A. Marsan, and G. P. Rossi, "Edge-based platoon control," *Comput. Commun.*, vol. 181, pp. 17–31, Jan. 2022.

[8] D. Pi, P. Xue, B. Xie, H. Wang, X. Tang, and X. Hu, "A platoon control method based on DMPC for connected energy-saving electric vehicles," *IEEE Trans. Transport. Electrific.*, vol. 8, no. 3, pp. 3219–3235, Sep. 2022.

[9] L. Zuo, Y. Zhang, M. Yan, and W. Ma, "Distributed integrated sliding mode-based nonlinear vehicle platoon control with quadratic spacing policy," *Complexity*, vol. 2020, pp. 1–9, Dec. 2020.

[10] X. Guo, J. Wang, F. Liao, and R. S. H. Teo, "Distributed adaptive sliding mode control strategy for vehicle-following systems with nonlinear acceleration uncertainties," *IEEE Trans. Veh. Technol.*, vol. 66, no. 2, pp. 981–991, Feb. 2017.

[11] Z. Shen, Y. Liu, Z. Li, and M. H. Nabin, "Cooperative spacing sampled control of vehicle platoon considering undirected topology and analog fading networks," *IEEE Trans. Intell. Transp. Syst.*, vol. 23, no. 10, pp. 18478–18491, Oct. 2022.

[12] Y. Zheng, S. E. Li, K. Li, and W. Ren, "Platooning of connected vehicles with undirected topologies: Robustness analysis and distributed $H_\infty$ controller synthesis," *IEEE Trans. Intell. Transp. Syst.*, vol. 19, no. 5, pp. 1353–1364, May 2018.

[13] L. Zhang, J. Sun, and G. Lai, "Event-based leader-follower consensus for linear multi-agent systems with adaptive weighting under directed communication topologies," in *Proc. 12th Asian Control Conf. (ASCC)*, Jun. 2019, pp. 925–930.

[14] G. Fiengo, D. G. Lui, A. Petrillo, S. Santini, and M. Tufo, "Distributed robust PID control for leader tracking in uncertain connected ground vehicles with V2V communication delay," *IEEE/ASME Trans. Mechatronics*, vol. 24, no. 3, pp. 1153–1165, Jun. 2019.

[15] U. Montanaro, G. Fiengo, A. Tufano, and S. Santini, "On the effectiveness of the extended cooperative adaptive control for vehicles platooning," in *Proc. Eur. Control Conf. (ECC)*, Aalborg, Denmark, Jun. 2016, pp. 2453–2458.

[16] J. Wang, H. Zheng, J. Guo, J. Fan, and K. Li, "Distributed adaptive robust $H_\infty$ control of intelligent-connected electric vehicles platooning subject to communication delay," *IET Intell. Transp. Syst.*, vol. 15, no. 5, pp. 699–711, May 2021.

[17] F. Gao, B. Liu, and J. Qi, "Distributed sliding-mode control for formation of multiple nonlinear autonomous vehicles coupled by uncertain topology," *Social Netw. Appl. Sci.*, vol. 1, no. 4, p. 374, Apr. 2019.

[18] K. Li, Y. Bian, S. E. Li, B. Xu, and J. Wang, "Distributed model predictive control of multi-vehicle systems with switching communication topologies," *Transp. Res. C, Emerg. Technol.*, vol. 118, Sep. 2020, Art. no. 102717.

[19] A. C. J. Luo, *Dynamical System Synchronization*. New York, NY, USA: Springer, 2013.

[20] Y. Wu, R. Lu, H. Su, P. Shi, and Z.-G. Wu, *Synchronization Control for Large-Scale Network Systems*. Cham, Switzerland: Springer, 2017.

[21] S. Dudhe, D. K. Dheer, and G. L. Raja, "A portable meconium aspirator with fractional augmented pressure control system," *IEEE Trans. Circuits Syst. II, Exp. Briefs*, vol. 72, no. 5, pp. 733–737, May 2025.

[22] U. Mehta, P. Aryan, and G. L. Raja, "Tri-parametric fractional-order controller design for integrating systems with time delay," *IEEE Trans. Circuits Syst. II, Exp. Briefs*, vol. 70, no. 11, pp. 4166–4170, Nov. 2023.

[23] A. Anand, N. Kumari, P. Aryan, and G. L. Raja, "EO optimized novel type-2 fuzzy ID-P controller for LFC of deregulated multi-area power system with robust stability analysis," in *Proc. 2nd Int. Conf. Power, Control Comput. Technol. (ICPC2T)*, Mar. 2022, pp. 1–6.

[24] P. Aryan and G. L. Raja, "Analysis of type-2 fuzzy ID$^\mu$-P controller for LFC with communication delay," in *Proc. IEEE Global Conf. Comput., Power Commun. Technol. (GlobConPT)*, Sep. 2022, pp. 1–7.

[25] D. Kumar, G. L. Raja, M. Alkhatib, and U. R. Muduli, "Enhancing LFC with relocated fractional IMC for power systems under communication latency," in *Proc. IEEE 4th Int. Conf. Sustain. Energy Future Electric Transp. (SEFET)*, Hyderabad, India, Jul. 2024, pp. 1–6, doi: 10.1109/sefet61574.2024.10717993.

[26] S. Kumari, P. Aryan, D. Kumar, and G. L. Raja, "Hybrid dual-loop control method for dead-time second-order unstable inverse-response plants with a case study on CSTR," *Int. J. Chem. React. Eng.*, vol. 20, no. 11, pp. 1381–1391, May 2022.

[27] D. Mukherjee, G. L. Raja, P. Kundu, and A. Ghosh, "Design of optimal fractional order Lyapunov based model reference adaptive control scheme for CSTR," *IFAC-PapersOnLine*, vol. 55, no. 1, pp. 436–441, 2022.

[28] D. Kumar and G. L. Raja, "Unified fractional indirect IMC-based hybrid dual-loop strategy for unstable and integrating type CSTRs," *Int. J. Chem. React. Eng.*, vol. 21, no. 3, pp. 251–272, Aug. 2022.

[29] O. Hanif, S. Tiwari, and V. Kumar, "Modelling and control of a nonlinear distillation column: A, using fractional-order controllers," in *Proc. IEEE 18th India Council Int. Conf. (INDICON)*, Guwahati, India, Dec. 2021, pp. 1–7, doi: 10.1109/INDICON52576.2021.9691748.

[30] P. Aryan, G. L. Raja, and U. Mehta, "FOI$^{\lambda}$D$^{1-\lambda}$ controller: An alternative to double-loop control schemes for integrating processes," in *Proc. IEEE 3rd Int. Conf. Smart Technol. Power, Energy Control (STPEC)*, Dec. 2023, pp. 1–6.

[31] D. Das, S. Chakraborty, U. Mehta, and G. L. Raja, "Fractional dual-tilt control scheme for integrating time delay processes: Studied on a two-tank level system," *IEEE Access*, vol. 12, pp. 7479–7491, 2024.

[32] D. Mukherjee, G. L. Raja, P. Kundu, and A. Ghosh, "Analysis of improved fractional backstepping and Lyapunov strategies for stabilization of inverted pendulum," *Sādhanā*, vol. 49, no. 1, p. 48, Jan. 2024.

[33] B. J. Lurie, "Three-parameter tunable tilt-integral-derivative (TID) controller," *ISA Trans.*, vol. 33, no. 2, pp. 147–158, 1994.

[34] P. R. Sahu, K. Simhadri, B. Mohanty, P. K. Hota, A. Y. Abdelaziz, F. Albalawi, S. S. M. Ghoneim, and M. Elsisi, "Effective load frequency control of power system with two-degree freedom tilt-integral-derivative based on whale optimization algorithm," *Sustainability*, vol. 15, no. 2, p. 1515, Jan. 2023.

[35] Y. Luo and Y. Chen, "Fractional order [proportional derivative] controller for a class of fractional order systems," *Automatica*, vol. 45, no. 10, pp. 2446–2450, Oct. 2009.

[36] Y. Jin, Y.-Q. Chen, and D. Xue, "Time-constant robust analysis of a fractional order [proportional derivative] controller," *IET Control Theory Appl.*, vol. 5, no. 1, pp. 164–172, Jan. 2011.

[37] P. Chen, Y. Luo, Y. Peng, and Y. Q. Chen, "Optimal robust fractional-order PI$^{\lambda}$D controller synthesis for first-order-plus-time-delay systems," *ISA Trans.*, vol. 114, pp. 136–149, Jan. 2021.

[38] S. E. Hamamci, "Stabilisation using fractional-order PI and PID controllers," *Nonlinear Dyn.*, vol. 51, pp. 329–343, Oct. 2008.

[39] V. Shekher, P. Rai, and O. Prakash, "Tuning and analysis of fractional-order PID controller," *Int. J. Electron. Electr. Eng.*, vol. 5, no. 1, pp. 11–21, 2012.

[40] O. Hanif and R. S. Shree, "Design and analysis of proportional integral derivative controller and it's hybrids," in *Proc. IEEE 5th Int. Conf. Converg. Technol. (I2CT)*, Bombay, India, Mar. 2019, pp. 1–6, doi: 10.1109/i2ct45611.2019.9033684.

[41] O. Hanif and V. Kedia, "Evolution of proportional integral derivative controller," in *Proc. Int. Conf. Recent Innov. Electr., Electron. Commun. Eng. (ICRIEECE)*, Bhubaneswar, India, Jul. 2018, pp. 2655–2659, doi: 10.1109/ICRIEECE44171.2018.9008628.

[42] Z. A. Ansari and G. L. Raja, "Flow direction optimizer tuned robust FOPID-(1 + TD) cascade controller for oscillation mitigation in multi-area renewable integrated hybrid power system with hybrid electrical energy storage," *J. Energy Storage*, vol. 83, Apr. 2024, Art. no. 110616.

[43] W. Li, L. Shi, M. Shi, J. Yue, B. Lin, and K. Qin, "Analyzing containment control performance for fractional-order multi-agent systems via a delay margin perspective," *IEEE Trans. Netw. Sci. Eng.*, vol. 11, no. 3, pp. 2810–2821, May 2024.

[44] F. Sun, Y. Han, X. Wu, W. Zhu, and J. Kurths, "Group consensus of fractional-order heterogeneous multi-agent systems with random packet losses and communication delays," *Phys. A, Stat. Mech. Appl.*, vol. 636, Feb. 2024, Art. no. 129547.

[45] Y. Xie and Q. Ma, "Consensus analysis of fractional multi-agent systems with delayed distributed PI controller," *J. Syst. Sci. Complex.*, vol. 36, no. 1, pp. 205–221, Feb. 2023.

[46] E. Bahrampour, M. H. Asemani, M. Dehghani, and M. Tavazoei, "Consensus control of incommensurate fractional-order multi-agent systems: An LMI approach," *J. Franklin Inst.*, vol. 360, no. 6, pp. 4031–4055, Apr. 2023.

[47] R. Cajo, M. Guinaldo, E. Fabregas, S. Dormido, D. Plaza, R. De Keyser, and C. Ionescu, "Distributed formation control for multiagent systems using a fractional-order proportional–integral structure," *IEEE Trans. Control Syst. Technol.*, vol. 29, no. 6, pp. 2738–2745, Nov. 2021.

[48] R. Cajo, S. Zhao, D. Plaza, R. D. Keyser, and C. Ionescu, "Distributed control of second-order multi-agent systems: Fractional integral action and consensus," in *Proc. 39th Chin. Control Conf. (CCC)*, Jul. 2020, pp. 4652–4657.

[49] D. Yaylali, E. A. Butcher, and A. Dabiri, "Fractional PID consensus control protocols for second-order multiagent systems," in *Proc. AIAA Scitech Forum*, Jan. 2019, pp. 0656–0679.

[50] A. Y. Damani and P. Debbarma, "Formation control of nonholonomic wheeled mobile robots using adaptive distributed fractional-order fast-terminal sliding-mode control," *Arch. Mech. Eng.*, vol. 70, no. 4, pp. 567–587, 2023.

[51] A. Y. Damani, Z. A. Benselama, and R. Hedjar, "Formation control of nonholonomic wheeled mobile robots via fuzzy fractional-order integral sliding mode control," *Int. J. Dyn. Control*, vol. 11, no. 5, pp. 2273–2284, Oct. 2023.

[52] C. Flores, V. Milanés, and F. Nashashibi, "Using fractional calculus for cooperative car-following control," in *Proc. IEEE 19th Int. Conf. Intell. Transp. Syst. (ITSC)*, Nov. 2016, pp. 907–912.

[53] C. Flores, J. Muñoz, C. A. Monje, V. Milanés, and X.-Y. Lu, "Iso-damping fractional-order control for robust automated car-following," *J. Adv. Res.*, vol. 25, pp. 181–189, Sep. 2020.

[54] C. Flores and V. Milanés, "Fractional-order-based ACC/CACC algorithm for improving string stability," *Transp. Res. Part C: Emerg. Technol.*, vol. 95, pp. 381–393, Oct. 2018.

[55] S. Dadras, S. Dadras, and C. Winstead, "Resilient control design for vehicular platooning in an adversarial environment," in *Proc. Amer. Control Conf. (ACC)*, Jul. 2019, pp. 533–538.

[56] J. Wang, W. Hu, Y. Cui, W. Gu, R. Jiang, and Y. Yu, "Adaptive fractional-order PID controller design and parameter tuning for vehicle longitudinal control," in *Proc. Int. Conf. New Trends Comput. Intell. (NTCI)*, Oct. 2024, pp. 417–421.

[57] S. E. Li, Y. Zheng, K. Li, and J. Wang, "An overview of vehicular platoon control under the four-component framework," in *Proc. IEEE Intell. Vehicles Symp. (IV)*, Jun. 2015, pp. 286–291.

[58] A. Sorniotti, S. De Pinto, S. Pragalathan, S. Dixit, S. Creighton, M. Wroblewski, and U. Montanaro, "Linearising longitudinal vehicle dynamics through adaptive control techniques for platooning applications," *Int. J. Powertrains*, vol. 10, no. 4, pp. 312–336, 2021.

[59] A. Coppola, D. G. Lui, A. Petrillo, and S. Santini, "Distributed fixed-time leader-tracking control for heterogeneous uncertain autonomous connected vehicles platoons," in *Proc. 29th Medit. Conf. Control Autom. (MED)*, Jun. 2021, pp. 554–559.

[60] J. Feng, Z. Gao, and B. Guo, "State-feedback and nonsmooth controller design for truck platoon subject to uncertainties and disturbances," *World Electric Vehicle J.*, vol. 15, no. 6, p. 251, Jun. 2024.

[61] Y. Li, Q. Lv, H. Zhu, H. Li, H. Li, S. Hu, S. Yu, and Y. Wang, "Variable time headway policy based platoon control for heterogeneous connected vehicles with external disturbances," *IEEE Trans. Intell. Transp. Syst.*, vol. 23, no. 11, pp. 21190–21200, Nov. 2022.

[62] K. Halder, U. Montanaro, S. Dixit, M. Dianati, A. Mouzakitis, and S. Fallah, "Distributed $H_{\infty}$ controller design and robustness analysis for vehicle platooning under random packet drop," *IEEE Trans. Intell. Transp. Syst.*, vol. 23, no. 5, pp. 4373–4386, May 2022.

[63] S. E. Li, X. Qin, Y. Zheng, J. Wang, K. Li, and H. Zhang, "Distributed platoon control under topologies with complex eigenvalues: Stability analysis and controller synthesis," *IEEE Trans. Control Syst. Technol.*, vol. 27, no. 1, pp. 206–220, Jan. 2019.

[64] Z. Zeng and T.-Y. Li, "A numerical method for computing the Jordan canonical form," 2021, *arXiv:2103.02086*.

[65] H. Guo and C.-L. Liu, "Observer-based consensus protocol of vehicles platooning with time delay," in *Proc. 33rd Chin. Control Decis. Conf. (CCDC)*, May 2021, pp. 4949–4954.

[66] Z. Zhang and X. Zhu, "Internal stability and string stability analysis for vehicle platoon with time delays via the distributed PID controller," in *Proc. 41st Chin. Control Conf. (CCC)*, Jul. 2022, pp. 49–54.

[67] A. Elahi, A. Alfi, and H. Modares, "Distributed consensus control of vehicular platooning under delay, packet dropout and noise: Relative state and relative input–output control strategies," *IEEE Trans. Intell. Transp. Syst.*, vol. 23, no. 11, pp. 20123–20133, Nov. 2022.

[68] A. Subhadarsini, B. Panda, and B. Nayak, "Maiden application and control-parameter sensitivity analysis of fractional-order tilt-integral-derivative controller in standalone solar photovoltaic system," *J. Renew. Energy Eng.*, vol. 9, no. 4, pp. 85–100, Dec. 2022.
[69] J. Gallier, "Spectral theory of unsigned and signed Graphs. Applications to graph clustering: A survey," 2016, *arXiv:1601.04692*.
[70] G. D. Medina, N. R. Ojeda, J. H. Pereira, and L. G. Romero, "Fractional Laplace transform and fractional calculus," *Int. Math. Forum*, vol. 12, no. 20, pp. 991–1000, 2017.
[71] R. K. H. Galvão, M. C. M. Teixeira, E. Assunção, H. M. Paiva, and S. Hadjiloucas, "Identification of fractional-order transfer functions using exponentially modulated signals with arbitrary excitation waveforms," *ISA Trans.*, vol. 103, pp. 10–18, Aug. 2020.
[72] X. Li, S. A. Evangelou, and R. Lot, "Integrated management of powertrain and engine cooling system for parallel hybrid electric vehicles," in *Proc. IEEE Vehicle Power Propuls. Conf. (VPPC)*, Aug. 2018, pp. 1–8.
[73] D. Huang, S. Li, Z. Zhang, Y. Liu, and B. Mi, "Design and analysis of longitudinal controller for the platoon with time-varying delay," *IEEE Trans. Intell. Transp. Syst.*, vol. 23, no. 12, pp. 23628–23639, Dec. 2022.
[74] A. Ghasemi and S. Rouhi, "A safe stable directional vehicular platoon," *Proc. Inst. Mech. Engineers, D, J. Automobile Eng.*, vol. 229, no. 8, pp. 1083–1093, Jul. 2015.
[75] S. Wen and G. Guo, "Sampled-data control for connected vehicles with Markovian switching topologies and communication delay," *IEEE Trans. Intell. Transp. Syst.*, vol. 21, no. 7, pp. 2930–2942, Jul. 2020.
[76] I. Podlubny, *Fractional Differential Equations*. San Diego, CA, USA: Academic, 1999.
[77] A. T. Azar, S. Vaidyanathan, and A. Ouannas, *Fractional-Order Control and Synchronisation of Chaotic Systems*. Cham, Switzerland: Springer, 2017.
[78] E. Çokmez and I. Kaya, "Stability boundary locus for unstable processes with time delay under fractional-order PI controllers," in *Proc. 6th Int. Conf. Control Eng. Inf. Technol. (CEIT)*, Oct. 2018, pp. 1–6.

**OMAR HANIF** (Graduate Student Member, IEEE) received the Bachelor of Technology (B.Tech.) degree in electrical engineering from Aligarh Muslim University (AMU), India, in 2015, the master's degree in systems and control engineering (formerly process control) from the National Institute of Technology (NIT), Warangal, India, in 2018, and the M.Sc. degree in advanced control systems engineering from The University of Manchester, U.K., in 2020. He is currently pursuing the Ph.D. degree with the University of Surrey, U.K. His research interests include systems control, fractional-order control, cooperative control of multi-agent systems, and vehicle platooning.

**PATRICK GRUBER** received the M.Sc. degree in motorsport engineering and management from Cranfield University, Cranfield, U.K., in 2005, and the Ph.D. degree in mechanical engineering from the University of Surrey, Guildford, U.K., in 2009. He is currently a Professor of advanced vehicle systems engineering with the University of Surrey. His research interests include vehicle dynamics and tire dynamics with special focus on friction behavior.

**ALDO SORNIOTTI** (Member, IEEE) received the M.Sc. degree in mechanical engineering and the Ph.D. degree in applied mechanics from the Politecnico di Torino, Turin, Italy, in 2001 and 2005, respectively. He is currently a Full Professor of applied mechanics with the Politecnico di Torino, after being a Professor of advanced vehicle engineering with the University of Surrey, Guildford, U.K., where he led the Centre for Automotive Engineering. His research interest includes vehicle dynamics control for electric and automated vehicles.

**UMBERTO MONTANARO** received the M.Sc. degree in computer science engineering and the Ph.D. degree in control engineering and mechanical engineering from the University of Naples Federico II, Naples, Italy, in 2005, 2009, and 2016, respectively. He is currently a Senior Lecturer in control engineering and autonomous systems with the University of Surrey, Guildford, U.K. Moreover, he is also the Founder and the Director of Surrey Team for the Control of Smart Multi-Agent Systems Operating Autonomously and Synergistically (Su-COSMOS). His research interests include adaptive control, and control of piecewise affine, mechatronic, automotive systems, and coordination of networked autonomous systems.